# Laser shockwave cleaning

Lammers, N.A.

*Award date:*
2008

# Laser Shockwave Cleaning

N.A. Lammers
Eindhoven, Januari 2008

EPG 08-02

ASML Supervisor:
Dr. Ir. A. Bleeker

TU\e Supervisor:
Prof. Dr. J.J.A.M. van der Mullen

University of Technology Eindhoven
Faculty of Applied Physics

# Abstract

At this moment the prime candidate for the next generation lithographic technique is Extreme UltraViolet (EUV) lithography. With EUV lithography it will be possible to produce integrated circuits with feature sizes of 32 nm and below. This capability to produce smaller feature sizes inherently means, that the role of particle contaminations on the reticle during exposure becomes increasingly important. In the case of EUV lithography, particles as small as 30 nm can already cause serious defects in the electronic components on an integrated circuit. Conventional cleaning methods (wet cleaning, megasonics) are not able to remove such small particles fast, reliably and without damage.

In search of a new cleaning method that can meet the new cleaning requirements, this thesis focuses on a novel cleaning method called *Laser Shockwave Cleaning* (LSC). Laser shockwave cleaning is a cleaning method which is based on the *Laser Induced Breakdown* (LIB) of gasses. The shockwave generated by the breakdown process is used to remove small particles from the contaminated surface.

To study its properties, the shockwave produced by the LIB was made visible with visualization techniques such as time resolved *shadowgraphy* and *Schlieren photography*. Amongst other things, the recorded images revealed the size and expansion velocity of the shockwave, which were found to be consistent with the *Taylor & Sedov* solution for point explosions. Combining the Taylor & Sedov solution with shock theory and adhesion theory, made it possible to develop a model that describes the removal of particles by LSC. The results produced by this model were later confirmed to be in agreement with the results of the particle removal experiments.

To asses the cleaning performance of LSC, a number of cleaning experiments were performed on unpatterned surfaces. The majority of these experiments were performed on 1" flat silicon wafers, which were contaminated with polysterene latex (PSL) spheres. These experiments showed that it was possible to reliably remove PSL spheres as small as 50 nm with LSC. This result proves the cleaning capabilities of LSC, and can be seen as a proof of concept for the method. The removal of 30 nm particles could not be achieved, but this is in agreement with the particle removal model developed earlier. The model predicts however, that under different circumstances (in the absence of capillary forces), it must be possible to remove particles smaller than 30 nm. It is therefore recommended to continue this research, to further ascertain the cleaning possibilities of LSC.

# Contents

# 1 Introduction

One of the most influential technological achievements of the 20$^{\text{th}}$ century is undoubtedly the development of the integrated circuit. By integrating a large collection of miniaturized electronic components onto a small piece of silicon, the integrated circuit made it possible to mass–produce small and reliable electronic computing devices. At the moment, the typical dimension of an electronic component on an integrated circuit has dropped well below 100 nm, and is expected to drop even further in the future. With such small dimensions, it is not surprising that the manufacturing process is highly sensitive to particle contaminations.

One of the manufacturing steps that is particularly vulnerable to particle contaminations is lithography. During manufacturing, lithography tools are used to print the pattern of the integrated circuit onto a silicon wafer. During this process the reticle is protected by a thin transparent pellicle, which acts as a physical barrier between the surface and the particles. Unfortunately, it has proven to be impossible to use the pellicles in the next generation Extreme UltraViolet (EUV) lithography tools. Therefore, the reticle is likely to be subjected to some degree of particle contamination. This poses a very serious problem, since the presence of one particle as small as 30 nm can ruin an entire batch of wafers.

Conventional cleaning methods (wet cleaning, megasonics) are not able to remove these small particles fast and reliably. In search of a new cleaning method that can meet the new cleaning requirements, this thesis focuses on a novel cleaning method called *Laser Shockwave Cleaning* (LSC). This particular cleaning method removes the particles by exposing them to a fast moving shockwave, which is generated by the *Laser Induced Breakdown* (LIB) of air.

## 1.1 Optical Lithography

In its original form, lithography is a printing technique developed by Alois Senefelder at the end of the 18$^{\text{th}}$ century. The name lithography is derived from the ancient Greek word *lithos*, which refers to the piece of limestone that was used in the printing process. By exploiting the hydrophobic/hydrophilic properties of the ink, it was possible to transfer the image from the limestone onto a piece of paper, or any other suitable flat surface.

The semiconductor industry uses a more sophisticated form of lithography to print the image of an integrated circuit onto a silicon wafer. This type of lithography is also refered to as optical lithography, since the image is transfered optically from the reticle onto the wafer. The reticle contains the master image of the integrated circuit, and the image is projected onto the wafer by the optical system depicted in figure 1.1. Since the reticle contains the image of the integrated circuit, it is imperative that the reticle is free of any contaminations that might cause imaging errors. The light that passes through the reticle is projected onto the wafer, which is coated with a photochemical substance called photoresist. After exposure, the exposed (or unexposed) parts of the photoresist are etched away. The result is a patterned layer of photoresist on the surface of the wafer, that can be used for further processing (e.g. etching or deposition). The entire process can be repeated several times to create an integrated circuit that consists of multiple

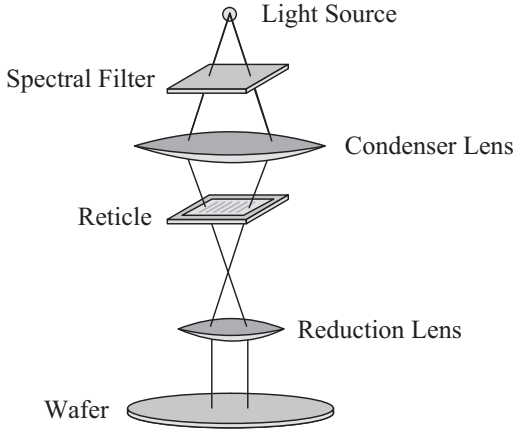


Figure 1.1: Schematic drawing of the projection optics used in lithography tools today. The pattern that is projected onto the wafer is generated by the reticle, which is a flat piece of quartz coated with a thin layer of chrome. The image of the integrated circuit has been etched into the chrome layer, which makes the reticle transparent at these specific locations.

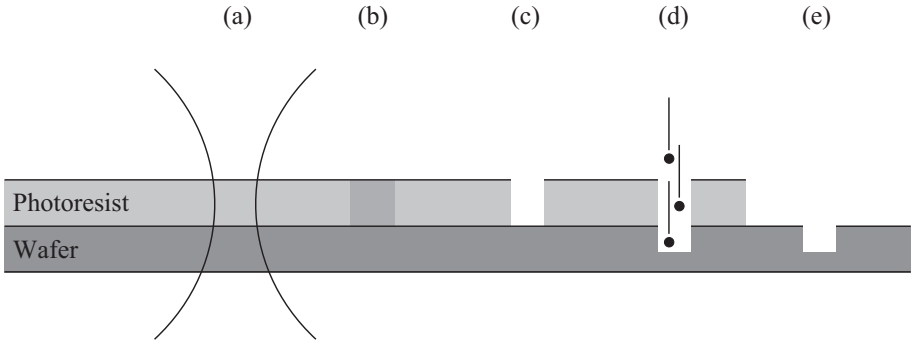


Figure 1.2: Simplified representation of a typical lithographic process. (a) The image of the integrated circuit is projected onto the coated wafer. (b) The exposed photoresist undergoes a chemical reaction. (c) The exposed (or sometimes unexposed) part of the photoresist is etched away. (d) This leaves a patterned surface of photoresist, which can be used for further processing (e.g. plasma etching or deposition). (e) The result is a patterned structure on the surface of the wafer.

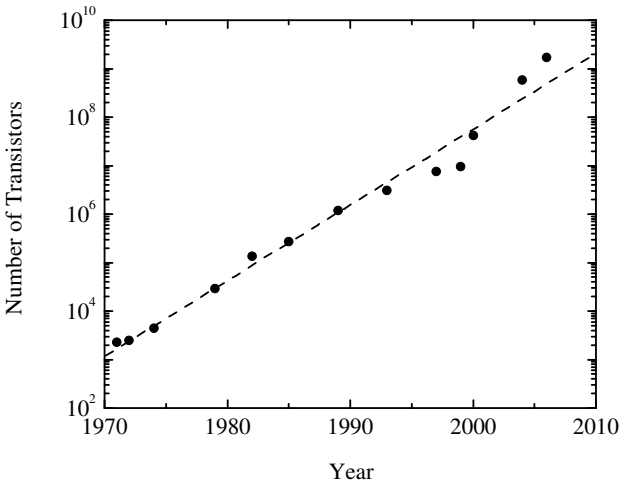


Figure 1.3: This graph shows that the number of transistors on Intel microprocessors has increased exponentially over the past few decades.

layers. The entire process has also been summarized in figure 1.2.

## 1.2 Resolution and Depth of Focus

In 1965 Gordon Moore [1] made his famous prediction that the number of transistors on an integrated circuit doubles every 18 months. This prediction is now commonly known as Moore's Law, and it has served as a guideline for the semiconductor industry during the past few decades. Figure 1.3 shows that the semiconductor industry has been successful in their efforts to keep pace with Moore's law, which can be attributed to the ongoing miniaturization of the electronic components on an integrated circuit.

Two important aspects that limit component miniaturization in lithography, are the *resolution* and *depth of focus* of the projected image. The resolution is defined as the minimum line width that can be projected onto the wafer, and the depth of focus gives the extent of the region around the image plane in which the image appears to be sharp. Both the resolution (RES) and the depth of focus (DOF) are bound by the laws of physics, and may be calculated with the following formulas [2]:

$$\text{RES} = k_1 \frac{\lambda}{\text{NA}}, \tag{1.1}$$

$$\text{DOF} = k_2 \frac{\lambda n}{\text{NA}^2}, \tag{1.2}$$

where $k_1$ and $k_2$ are process dependent factors, $\lambda$ the wavelength of the light, and NA the numerical aperture. The numerical aperture is a property of the projection optics, and can be calculated as follows:

$$\text{NA} = n \sin\theta, \tag{1.3}$$

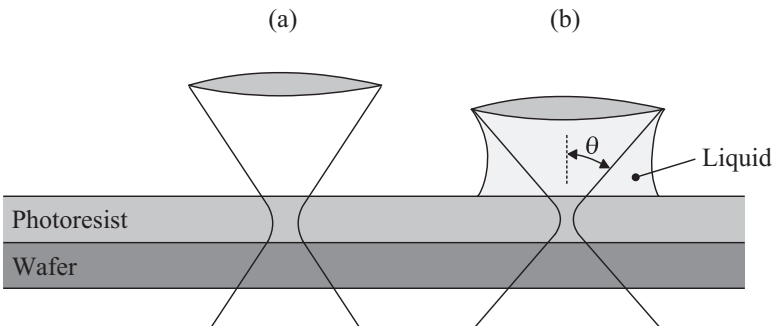


Figure 1.4: Principle of immersion lithography. (a) Normal exposure without immersion. (b) The introduction of a liquid between the lens and the wafer makes it possible to achieve a higher numerical aperture and a better resolution.

where $n$ is the refractive index of the medium between the lens and the wafer, and $\theta$ the half–angle of the maximum cone of light that can exit the projection optics.

Formulas (1.1–1.3) show that there are several possibilities to enhance the resolution: decrease the process dependent factor $k_1$, increase the numerical aperture, or decrease the wavelength. Today's state–of–the–art lithography tools use a technique called *immersion* to increase the numerical aperture. These tools are able to achieve a high numerical aperture by introducing a liquid between the projection optics and the wafer, as shown in figure 1.4. The liquid that is introduced between the lens and the wafer has a refractive index which is larger than that of the surrounding air. This causes the light to refract more sharply at the lens–liquid boundary, thus enabling a larger half–angle $\theta$ and a larger numerical aperture. Unfortunately, immersion lithography is almost stretched to its limits. Because the depth of focus decreases rapidly for high numerical apertures, it has become increasingly difficult to obtain a properly focused image. According to the International Technology Roadmap for Semiconductors [3] (ITRS), it is expected that it will be possible to produce 32 nm features in the year 2009. Since immersion lithography is probably not capable of producing such high resolutions, a new type of lithography is needed to meet this requirement. This new type of lithography will have to employ light with a considerably shorter wavelength than the 193 nm that is being used in immersion lithography today. The most promising candidate is Extreme UltraViolet (EUV) lithography, which uses extreme ultraviolet light with a wavelength of 13.5 nm to illuminate the wafer.

## 1.3 Extreme Ultraviolet Lithography

As discussed in the previous section, Extreme UltraViolet (EUV) lithography is the prime candidate for the next generation of lithography tools. This new technique uses light with a wavelength of 13.5 nm to achieve resolutions of 32 nm and below. Unfortunately, extreme ultraviolet radiation has a very short mean free path in almost all materials. It is therefore necessary to use reflective multilayer optics instead of transmissive optics, because most of the light would otherwise be absorbed by the optics. These reflective multilayer optics are specifically designed to reflect EUV light with a wavelength of 13.5 nm, as can be seen in figure 1.5.

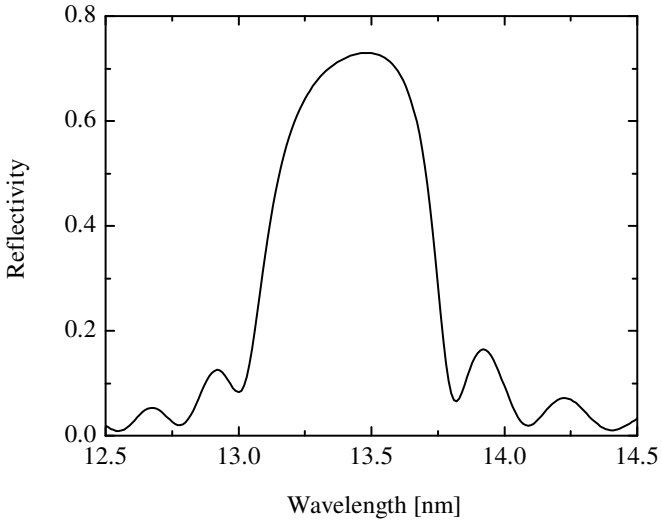


Figure 1.5: Calculated reflectivity of an EUV multilayer mirror consisting of 40 Si-Mo bilayers with a thickness of 6.9 nm [4]. This results in an optimal reflection in a narrow wavelength band around 13.5 nm.

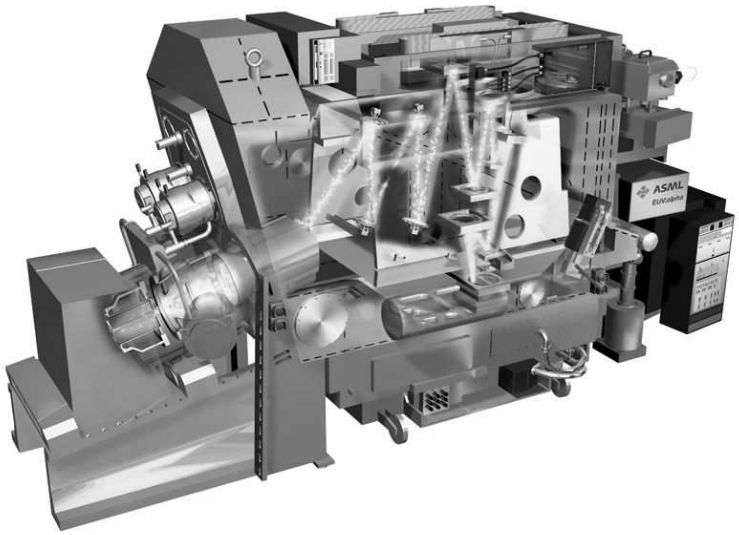


Figure 1.6: Exploded view of the ASML EUV alpha tool. The EUV light that is produced by the plasma light source is shaped and redirected via multilayer mirrors towards a reflective multilayer reticle, which projects the image onto the wafer.

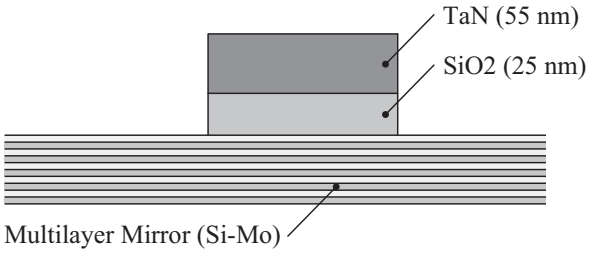


Figure 1.7: Cross sectional view of an EUV reticle. The EUV reticle consists of an absorbing $SiO_2$/TaN bilayer on top of a Si–Mo multilayer mirror.

| **Particle Contamination** | **Chemical Contamination** |
|---|---|
| Skin flakes | Lubricants |
| Fibres | Adhesives |
| Saliva | Cleaning agents |
| Cosmetics | Outgassing of plastics |
| Metal particles | Skin grease |
| Smoke | Transpiration |
| Pollen | Finger prints |
| Sand | Saliva |
| | Cosmetics |

Table 1.1: List of common particle and chemical contaminations. Some types of contamination fall into both categories.

Figure 1.6 shows a drawing of the EUV alpha tool built by ASML. The extreme ultraviolet light is produced by a plasma light source located at the left hand side of the lithography machine. This beam of light is reshaped and redirected towards the reticle, which projects the image onto the wafer. The reticle is also a multilayer mirror, that is coated with an absorbing layer. The pattern itself is etched into the absorbing layer, thereby exposing the reflective multilayer mirror underneath. Figure 1.7 shows the cross section of an EUV reticle. The whole system is operated under vacuum conditions, since most gasses at atmospheric pressure also strongly absorb EUV radiation. The pressure at the exposure position is typically in the order of $10^{-1}$ mbar $H_2$ to circumvent this problem.

An important issue, that can have a large effect on the performance of (EUV) lithography tools, is the presence of contaminations. Contaminations can be harmful to the functionality or reliability of the lithography tool or one of its subsystems. There are two distinct types of contaminations: particle and chemical contaminations. Examples of particle contaminations are skin flakes or fibres, such as hair or clothing. Chemical contaminations are caused by exposure to contaminated gasses or fluids, which can lead to film like deposits on exposed surfaces. Table 1.1 gives a list of examples of both particle and chemical contaminations. Note that some contaminations, such as cosmetics, fall into both categories of contamination.

The presence of particles on the surface of the reticle can lead to serious imaging errors. To counteract this problem, very thin transparent pellicles are normally used to

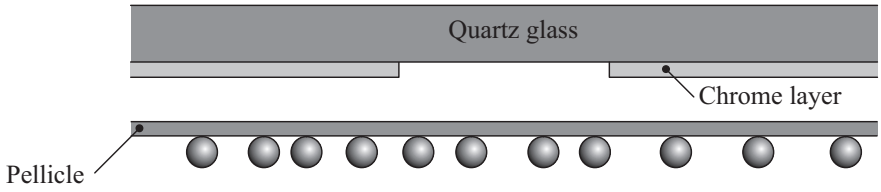


Figure 1.8: Schematic drawing that explains the function of the pellicle. The pellicle is located underneath the reticle to prevent particles from settling on the surface. This keeps the particles out of focus, and reduces the chance of imaging errors due to particles.

protect the surface of the reticle. As can be seen in figure 1.8, the pellicle is located a small distance underneath the reticle. This ensures that the particles do not come into contact with the reticle and are kept out of focus. Unfortunately it is almost impossible to apply this technology to EUV lithography, because the pellicle absorbs too much EUV radiation. Since EUV reticles need to be operated without a pellicle, they are more likely to be exposed to organic and inorganic particle contaminations. Therefore a fast and reliable cleaning process is needed to remove particles as small as 30 nm from the surface of the reticle. One possible method is Laser Shockwave Cleaning (LSC), which will be investigated in more detail in the next section and the following chapters.

## 1.4 Laser Shockwave Cleaning

*Laser Shockwave Cleaning* (LSC) removes particles by exposing them to a fast moving shockwave, which is generated by the *Laser Induced Breakdown* (LIB) of air. LIB can be achieved by exposing the air to the field of a very intense electromagnetic wave. This is done by focusing the light of a high energy laser pulse into a very small volume. The subsequent point explosion generates a shockwave, which is used to remove small particles from the contaminated surface. Figure 1.9 shows a schematic drawing of the cleaning process.

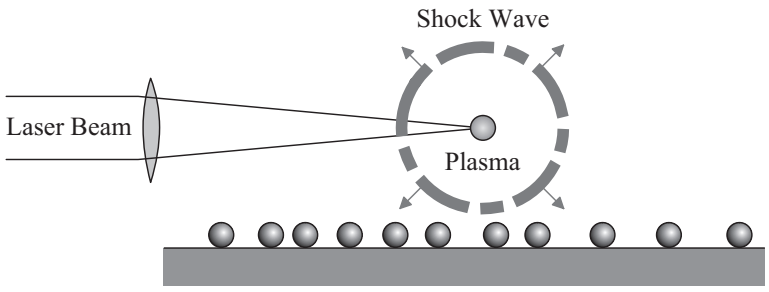


Figure 1.9: Laser Shockwave Cleaning (LSC). The focused laser pulse creates a small plasma above the contaminated surface. The plasma expands at such a high rate that it generates a shockwave. The shockwave is used to remove the particles from the contaminated surface.

Laser shockwave cleaning has recently gained a lot of interest as a cleaning method for EUV reticles, because the convential cleaning methods (wet cleaning, chemical cleaning,

megasonics, and $CO_2$ cleaning) are unable to meet the new cleaning requirements. These requirements include the removal of 30 nm particles without any damage to the surface of the reticle. Furthermore, the cleaning process must not contaminate the vacuum environment of the EUV lithography tool, which means that wet and chemical cleaning processes are at a disadvantage. In addition to these already demanding requirements, the cleaning process must also be as fast as possible to minimize the downtime of the lithography tool.

## 1.5 Outline and Focus of this Thesis

The main focus of this thesis will be on the feasibility of Laser Shockwave Cleaning (LSC) as a method for particle removal from EUV reticles. The next chapter of this thesis will give a short explanation of the theoretical background of laser produced plasmas and the shockwaves that they create. This chapter is followed by chapter 3, which investigates the transient behavior of the shockwave with techniques such as shadowgraphy and Schlieren photography. In chapter 4 the physics of particle adhesion and removal will be discussed. During this discussion the main adhesion forces will be identified, and the chapter is concluded with the presentation of a particle removal model. Chapter 5 will continue with the results of the cleaning experiments that were performed to assess the cleaning capabilities of the LSC method. This thesis is concluded with chapter 6, which contains the conclusions, as well as some remarks and recommendations for future research.

# 2 Laser Produced Plasma Shockwaves

This chapter will discuss the physical processes that lead to the generation of laser produced plasma shockwaves. The first section will discuss the properties and physics of laser produced plasmas, with a focus on the ionization mechanisms that are responsible for the breakdown process. The second section of this chapter will focus on the properties of the shockwave that is generated by laser induced breakdown. The shock theory presented here will primarily focus on point explosions, since laser induced breakdown is characterized by the almost instantaneous release of a relatively large amount of energy in a very small volume.

## 2.1 Laser Induced Breakdown (LIB)

Every cleaning step during the LSC process starts with the *Laser Induced Breakdown* (LIB) of air by a focused high energy laser pulse. The intense electromagnetic field of the laser pulse ionizes the air, and a plasma is created at the focal point of the lens. The properties of this plasma differ significantly from those of ordinary air, and will be discussed in the following subsection. After a general introduction into (laser produced) plasmas in subsection 2.1.1, the next three subsections wil give a more elaborate discription of the main ionization mechanisms during LIB: *Multi Photon Ionization* (MPI), *tunneling* and *Inverse Bremsstrahlung* (IB).

### 2.1.1 Plasma Characteristics

Plasmas are ionized gasses, and are therefore characterized by the presence of charged particles. Because of their unique physical properties, plasmas are often called the fourth state of matter. The presence of charged particles is what gives the plasma its unique properties, and sets it apart from ordinary non–ionized gasses. The separation of the charged particles in the plasma produces electric fields, and the flow of charged particles gives rise to currents and magnetic fields. These electric and magnetic fields allow the charged particles in the plasma to interact over much longer distances than the particles in ordinary non-ionized gasses. It should be noted however, that the plasma as a whole remains electrically neutral. This concept is called quasineutrality, and it can be defined as follows:

$$n_\mathrm{e} = \sum_\mathrm{i} n_\mathrm{i} Z_\mathrm{i}, \tag{2.1}$$

where $n_\mathrm{e}$ is the electron density, $n_\mathrm{i}$ the ion density, and $Z_\mathrm{i}$ the charge number.

The most important parameter for any plasma is the electron density $n_\mathrm{e}$. The second most important parameter is the electron temperature $T_\mathrm{e}$, which is often expressed in electron volts (1 eV = 11600 K). With these two parameters it is possible to classify the various types of plasma, as can be seen in figure 2.1. The diagram shows that laser produced plasmas, which are of particular importance to this thesis, have a high electron density and a moderate electron temperature. Another important plasma parameter is the ionization ratio, which is defined as the ratio between the electron density $n_\mathrm{e}$ and the

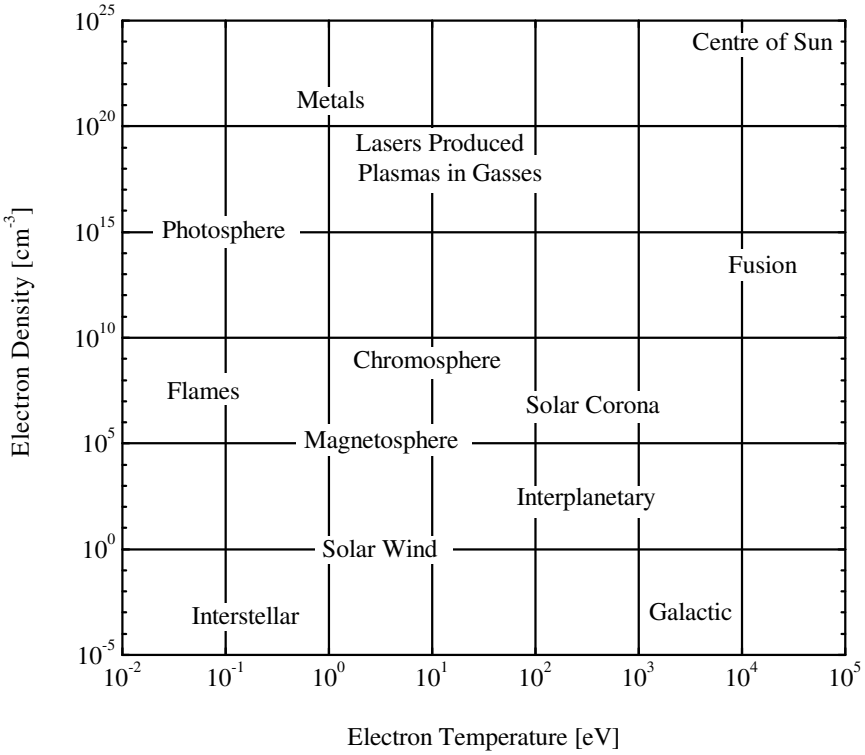


Figure 2.1: Classification diagram of plasmas according to their two most important plasma parameters: the electron density and the electron temperature [5].

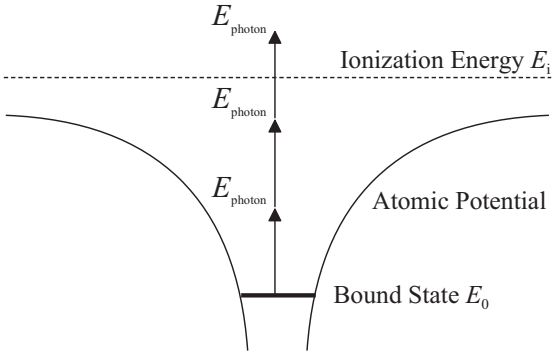


Figure 2.2: The bound electron can escape the atomic potential by absorbing multiple photons. This process is called multi photon ionization.

neutral density $n_a$. For most plasmas it can be estimated with the following approximate expression [6]:

$$\frac{n_e}{n_a} \approx \left(10^{-18} n_e\right)^{1/2}, \qquad [n_e] = \mathrm{cm}^{-3}. \tag{2.2}$$

This expression also holds for laser produced plasmas, and after inserting the appropriate electron density of $10^{20}$ cm$^{-3}$, this expression yields an ionization ratio of $10^2$. Laser produced plasmas are thus well ionized plasmas.

### 2.1.2 Multi Photon Ionization

In general there are three mechanisms responsible for the LIB of gasses: *Multi Photon Ionization* (MPI), *tunneling* and *Inverse Bremsstrahlung* (IB). The first two of these processes are self sufficient, whereas the third process always needs at least one free electron in the focal volume during the arrival of the laser pulse. The probability that such a free electron is produced by natural background radiation is however negligible [7]. Direct photoionization of the gas is also not possible, because the photon energy is typically less than the ionization energy. The formation of the first free electron in the focal volume must therefore involve the absorption of multiple photons, hence the name Multi Photon Ionization (MPI).

Figure 2.2 shows a schematic sketch of the MPI process. After absorbing one photon, the electron makes the transition from the bound state into a so called virtual state. The lifetime of this first virtual state is extremely short ($10^{-15}$ s), and can be calculated with Heisenbergs theorem:

$$\Delta t_1 \leq \frac{h}{E_{\mathrm{photon}}} = \frac{1}{\nu}, \tag{2.3}$$

where $h$ is Plancks constant, $E_{\mathrm{photon}}$ the photon energy, and $\nu$ the frequency of the photon. The electron in the first virtual state can be excited to the second virtual state by absorbing another photon. The lifetime of the second virtual state is however different from the first virtual state, namely:

$$\Delta t_2 \leq \frac{h}{2E_{\mathrm{photon}}} = \frac{1}{2\nu}. \tag{2.4}$$

This process can continue until the electron has gained enough energy to reach the ionized state.

Since the lifetimes of the virtual states are extremely short, a very high photon flux density is needed for MPI. Morgan [7] gives a simple expression for the ionization rate $W$ per atom as a function of the photon flux density $F$:

$$W = \frac{\sigma^k F^k}{\nu^{k-1}\,(k-1)!}, \qquad [W] = \mathrm{s}^{-1}, \qquad [F] = \mathrm{m}^{-2}\mathrm{s}^{-1}, \tag{2.5}$$

where $\sigma$ is the photon absorption cross section, $\nu$ the frequency of the incident electromagnetic wave, and $k$ the minimum number of photons that have to be absorbed to achieve ionization. Now suppose that the photon flux is passing through a volume $V$ of gas with pressure $p$. The number of atoms inside the volume may be calculated with the ideal gas law:

$$N_0 = \frac{pV}{RT} N_A, \tag{2.6}$$

where $R$ is the gas constant, $T$ the temperature and $N_A$ Avogadros number. The number of ionizations $N_i$ produced by a laser pulse of duration $\tau$ can be expressed as:

$$N_i = N_0 W \tau = \frac{pV N_A \sigma^k F^k \tau}{RT\nu^{k-1}\,(k-1)!}. \tag{2.7}$$

From this equation the flux density necessary to ionize one single atom can be calculated in a straightforward manner:

$$F_1 = \frac{\nu}{\sigma}\left[\frac{RT\,(k-1)!}{pV N_A \nu \tau}\right]^{1/k}. \tag{2.8}$$

When the condition for the onset of breakdown is set to the ionization of $N_c$ atoms per laser pulse, the breakdown threshold photon flux can be calculated with:

$$F_{\mathrm{th}} = \frac{\nu}{\sigma}\left[\frac{RT N_c\,(k-1)!}{pV N_A \nu \tau}\right]^{1/k}. \tag{2.9}$$

When it is assumed that breakdown occurs at an ionization fraction of $\delta = N_c/N_0$, the threshold photon flux can be rewritten into:

$$F_{\mathrm{th}} = \frac{\nu}{\sigma}\left[\frac{\delta\,(k-1)!}{\nu\tau}\right]^{1/k}. \tag{2.10}$$

This leads to the following expression for the threshold intensity:

$$I_{\mathrm{th}} = \frac{h\nu^2}{\sigma}\left[\frac{\delta\,(k-1)!}{\nu\tau}\right]^{1/k}, \qquad [I_{\mathrm{th}}] = \mathrm{W}\mathrm{m}^{-2}, \tag{2.11}$$

where $h$ is the Planck constant. Filling in typical values for all the parameters in equation (2.11) yields threshold intensities in the order of $(10^{12}$–$10^{13})$ W/cm$^2$. Such high intensities can be achieved by focusing the light of a high energy laser pulse into a very small focal point.

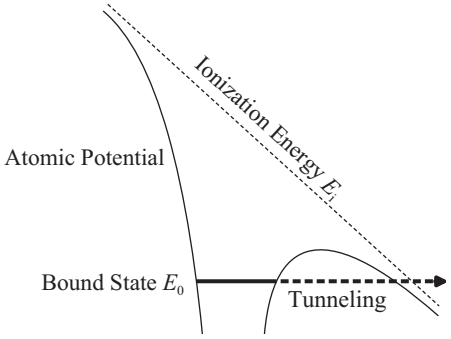


Figure 2.3: Schematic drawing of ionization by tunneling. The electric field of the laser radiation tilts the atomic potential, which makes ionization by tunneling possible. The tunneling occurs through (or even over) the reduced energy barrier.

### 2.1.3 Tunneling

The second ionization mechanism that can be of importance to the initiation of LIB is called *tunneling*. Tunneling occurs when the electric field of the laser radiation is strong enough to shift the bound states of the atoms in the gas. This energy shift is known as the AC–Stark shift, and its influence on the most weakly bound states can be significant. The result is a tilted atomic potential as sketched in figure 2.3, which makes it possible for an electron to tunnel from a bound state to a free state. An expression for the threshold intensity necessary for tunneling to become important is given by [8]:

$$I_{\mathrm{th}} = 4 \cdot 10^9 \left( \frac{E_{\mathrm{i}}^4}{Z^2} \right), \qquad [\mathrm{I_{th}}] = \mathrm{W/cm^2}, \qquad [E_{\mathrm{i}}] = \mathrm{eV}, \tag{2.12}$$

where $Z$ is the ion charge after ionization, and $E_{\mathrm{i}}$ is the corresponding ionization potential. Filling in typical values yields a threshold intensity in the order of ($10^{14}$–$10^{15}$) W/cm$^2$, which is considerably higher than the threshold intensity found for MPI.

### 2.1.4 Inverse Bremsstrahlung

After the initial phase of MPI and tunneling, the process of *cascade ionization* becomes more dominant. The free electrons produced by the MPI process are now able to absorb energy from the laser light via *Inverse Bremsstrahlung* (IB). Because of momentum conservation, the absorption of a photon by an electron must occur in the presence of an ion, which can carry the excess momentum. If the intensity and duration of the laser pulse are large enough, these electrons can gain enough energy to ionize other atoms by impact. This produces more electrons, which are also capable of ionizing other atoms. This process is called cascade ionization.

The strength of the IB absorption depends on the properties of the plasma and the incident laser light. The amount of intensity lost due to IB at each point along the beam path can be calculated with the following expression:

$$\mathrm{d}I(z) = -k_{\mathrm{IB}}(\lambda, z) I(z)\, \mathrm{d}z, \tag{2.13}$$

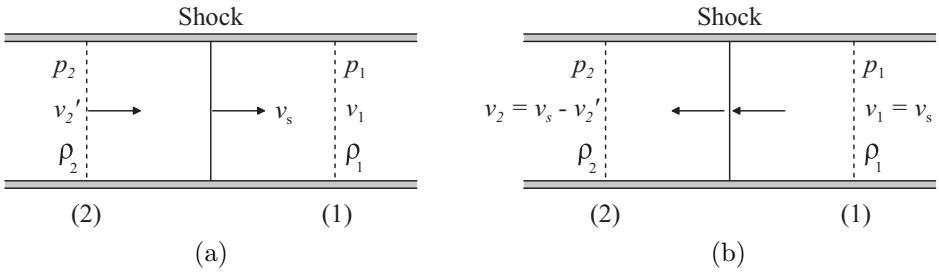


Figure 2.4: Planar shock front in (a) laboratory-fixed coordinates, and (b) shock-fixed coordinates.

where $I(z)$ is the intensity at position $z$, and $k_{\mathrm{IB}}(\lambda, z)$ the absorption coefficient for IB. The absorption coefficient $k_{\mathrm{IB}}$ can be calculated in the following way [9]:

$$k_{\mathrm{IB}} = \frac{13.49}{\lambda^2}\bar{Z}\left(\frac{n_{\mathrm{e}}}{n_{\mathrm{c}}}\right)^2 \frac{\ln\Lambda}{\sqrt{1-\frac{n_{\mathrm{e}}}{n_{\mathrm{c}}}}}\frac{1}{T_{\mathrm{e}}^{3/2}}, \tag{2.14}$$

where $\lambda$ is the wavelength of the laser light, $\bar{Z}$ the average charge state, $n_{\mathrm{e}}$ the electron density, $n_{\mathrm{c}}$ the critical electron density, $\ln\Lambda$ the Coulomb logarithm, and $T_{\mathrm{e}}$ the electron temperature. The critical electron density is defined as $n_{\mathrm{c}} = m\epsilon_0\omega^2/e^2$, where $m$ is the electron mass, $\epsilon_0$ the permittivity of vacuum, $\omega$ the angular frequency of the laser light, and $e$ the electron charge. Equation (2.14) shows that the absorption coefficient depends strongly on the electron density, and that its maximum value is found when the electron density approaches the critical electron density. However, for a wavelength of approximately 1 $\mu$m, the critical electron density is in the order of $10^{21}$ cm$^{-3}$, which is well above the electron density of laser produced plasmas in air. In this case, the inverse Bremsstrahlung coefficient will roughly scale with $n_{\mathrm{e}}^2$.

## 2.2 Shock Theory

The main characteristic of any explosion is the sudden release of a large amount of energy within a very small volume. This description of an explosion also applies to the laser induced breakdown process typically encountered in laser shockwave cleaning. In the case of laser shockwave cleaning, the focal volume is sufficiently small to consider the explosion a point explosion. The next few subsections will discuss the properties of the shockwave that such a point explosion produces.

### 2.2.1 Shock Relations

The LIB during the LSC process generates a high pressure bubble of air, which expands at a supersonic velocity. The expansion velocity is thus higher than the velocity at which information about the expanding bubble can propagate through the surrounding air. This means that the surrounding air is unable to react to the expanding bubble before it arrives, and is therefore swept away by the expanding bubble itself. The boundary between the surrounding air and the air that has been swept away is called the shock front. The shock front is characterized by very abrupt changes in the density, pressure, and velocity of the

air over a very short distance. The thickness of the shockfront is comparable to the mean free path $\bar{\lambda}$, and is given by [10]:

$$\delta \approx \frac{\bar{\lambda}}{M}. \tag{2.15}$$

where $M$ is the Mach number of the shockwave. The Mach number $M$ can be obtained by scaling the velocity of the shockwave with the speed of sound in the undisturbed medium:

$$M = v/c, \tag{2.16}$$

where $v$ is the velocity of the shock front, and $c$ the speed of sound in the undisturbed medium.

Figure 2.4 shows an example of a planar shock front in both laboratory and shock–fixed coordinates. Here it is assumed that the properties of the air jump discontinuously at the shock front, and that they have steady values in the regions before and after the shock front. Applying the principles of conservation of mass, momentum, and energy to the shock–fixed coordinate system in figure 2.4b yields:

$$\rho_1 v_\mathrm{s} = \rho_2 v_2, \tag{2.17}$$
$$p_1 + \rho_1 v_\mathrm{s}^2 = p_2 + \rho_2 v_2^2, \tag{2.18}$$
$$h_1 + v_\mathrm{s}^2/2 = h_2 + v_2^2/2, \tag{2.19}$$

where $p$ is the pressure, $\rho$ the density, $v$ the velocity, and $h$ the specific enthalpy. In addition to these conservation laws, the ideal gas law can be assumed to be valid for the strength of shocks typically encountered with strong explosions [11]:

$$p = \rho \frac{R}{m} T = \rho \bar{R} T, \tag{2.20}$$

where $R$ is the ideal gas constant, $\bar{R}$ the specific gas constant, $m$ the molar mass, and $T$ the temperature. When it is also assumed that the gas is perfect (constant specific heat capacities $c_\mathrm{p}$ and $c_\mathrm{v}$), than it is possible to write down the following equations of state:

$$p_1 = \frac{\gamma - 1}{\gamma} \rho_1 h_1, \tag{2.21}$$
$$p_2 = \frac{\gamma - 1}{\gamma} \rho_2 h_2, \tag{2.22}$$

where $\gamma = c_\mathrm{p}/c_\mathrm{v}$. Combining equations (2.17)–(2.22) yields the following shock relations, which describe the downstream flow quantities (2) as a function of their upstream counterparts (1):

$$\frac{p_2}{p_1} = 1 + \frac{2\gamma\left(M^2 - 1\right)}{\gamma + 1}, \tag{2.23}$$
$$\frac{T_2}{T_1} = \left(1 + \frac{2\gamma\left(M^2 - 1\right)}{\gamma + 1}\right) \frac{2 + (\gamma - 1) M^2}{(\gamma + 1) M^2}, \tag{2.24}$$
$$\frac{\rho_2}{\rho_1} = \frac{(\gamma + 1) M^2}{(\gamma - 1) M^2 + 2}, \tag{2.25}$$

| $\gamma$ | 6/5 | 7/5 | 5/3 |
|---|---|---|---|
| $Y(\gamma)$ | 0.90 | 1.03 | 1.15 |
| $Y^5(\gamma)/(\gamma+1)$ | 0.25 | 0.48 | 0.84 |

Table 2.1: Typical values of the dimensionless parameter $Y$ in the Taylor & Sedov solution.

where $M = v_1/c_1$ is the Mach number of the upstream flow. Finally, it should be noted that the shock relations (2.23)–(2.25) are only applicable to supersonic flows ($M \geq 1$). This can be illustrated by looking at the entropy change across the shock front [12]:

$$s_2 - s_1 = c_\mathrm{p} \ln\left(\frac{T_2}{T_1}\right) - \bar{R} \ln\left(\frac{p_2}{p_1}\right), \tag{2.26}$$

where $c_\mathrm{p}$ is the specific heat capacity at constant pressure. For subsonic flows ($M < 1$) this equation yields negative entropy changes, which is in violation of the second law of thermodynamics.

### 2.2.2 Spherical Shock

The LIB produced by the focused laser pulse creates a point explosion at the focal point of the convex lens. The point explosion produces a spherically expanding shockwave with radius $r_s$, which can be calculated with the Taylor & Sedov solution [13]:

$$r_\mathrm{s}(t) = t^{2/5} \left(\frac{W}{\rho_1}\right)^{1/5} Y(\gamma), \tag{2.27}$$

where $W$ is the energy of the laser pulse, $\rho_1$ the density of the undisturbed medium, and $\gamma$ the specific heat ratio of the medium. The dimensionless parameter $Y$ is an empirical constant, which depends on the specific heat ratio $\gamma$. Typical values of $Y$ are listed in table 2.1. With the help of the ideal gas law in equation (2.20) it is possible to rewrite equation (2.27) into:

$$r_\mathrm{s}(t) = t^{2/5} \left(\frac{W\bar{R}T_1}{p_1}\right)^{1/5} Y(\gamma), \tag{2.28}$$

where $\bar{R}$ is the specific gas constant, and $T_1$ the temperature of the undisturbed medium. The velocity of the shockwave can be calculated from equation (2.28) in a relatively straightforward manner:

$$v_\mathrm{s}(t) = \frac{d}{dt} r_s(t) = \frac{2}{5} t^{-3/5} \left(\frac{W\bar{R}T_1}{p_1}\right)^{1/5} Y(\gamma). \tag{2.29}$$

The Mach number $M_\mathrm{s}$ of the shockwave is obtained by scaling equation (2.29) with the speed of sound in the undisturbed medium. This gives the following expression:

$$M_\mathrm{s}(t) = \frac{v_s(t)}{\sqrt{\gamma\bar{R}T_1}} = \left(\frac{2}{5\sqrt{\gamma\bar{R}T_1}}\right) t^{-3/5} \left(\frac{W\bar{R}T_1}{p_1}\right)^{1/5} Y(\gamma), \tag{2.30}$$

where the speed of sound in the undisturbed medium is given by $\sqrt{\gamma \bar{R} T_1}$. Inserting equation (2.30) into shock relation (2.23) gives the following expression for the pressure in the disturbed medium:

$$p_2 = \frac{p_1}{\gamma + 1} \left\{ \frac{8}{25} \left( \bar{R} T_1 \right)^{-3/5} \left( \frac{W}{p_1} \right)^{2/5} Y^2 \left( \gamma \right) t^{-6/5} - \left( \gamma - 1 \right) \right\}. \tag{2.31}$$

Combining this equation with equation (2.28) gives the pressure of the disturbed medium as a function of the shockwave radius:

$$p_2 = \frac{p_1}{\gamma + 1} \left\{ \frac{8}{25} \left( \frac{W}{p_1} \right) \frac{1}{r_s^3} Y^5 \left( \gamma \right) - \left( \gamma - 1 \right) \right\}. \tag{2.32}$$

With this equation it is now possible to find an expression for the pressure jump $\Delta p$ across the shockwave:

$$\Delta p = p_2 - p_1 = \frac{8}{25} \left( \frac{1}{\gamma + 1} \right) \left( \frac{W}{r_s^3} \right) Y^5 \left( \gamma \right) - \left( \frac{2\gamma}{\gamma + 1} \right) p_1. \tag{2.33}$$

This equation is only valid in the case of strong shocks (small values of $r_s$) to which the Taylor & Sedov [13] solution applies. Equation (2.33) is therefore only valid for small values of $r_s$, which leads to the following simplification:

$$\Delta p = \frac{8}{25} \left( \frac{1}{\gamma + 1} \right) \left( \frac{W}{r_s^3} \right) Y^5 \left( \gamma \right). \tag{2.34}$$

Equation (2.34) is important for the optimization of the laser shockwave cleaning process, since the pressure jump across the shockwave is a direct measure of the cleaning force. It shows that the largest improvement in cleaning can be made by decreasing the distance between the laser focus and the surface that needs to be cleaned. This so–called *gap distance* is however limited to a minimum value, to avoid damage to the surface that needs to be cleaned. Another large improvement can be made by increasing the energy of the laser pulse, but it should be noted that in this case a larger gap distance is needed to avoid damage to the surface. It also shows that it is possible to increase the pressure jump marginally by switching to a medium with a higher specific heat ratio than air (e.g. helium or argon).

Equation (2.34) is only valid in the near field, where the shockwave travels with a velocity well above the speed of sound. In the far field the shockwave slows down, and begins to behave as a sound wave. The propagation of a sound wave is described by the well–known wave equation:

$$\frac{\partial^2 p}{\partial t^2} = c^2 \nabla^2 p, \tag{2.35}$$

where $p$ is the pressure, $c$ the speed of sound, and $t$ denotes the time. For spherically symmetric cases the wave equation can be rewritten into:

$$\frac{\partial^2 p}{\partial t^2} - c^2 \left( \frac{\partial^2 p}{\partial r^2} + \frac{2}{r} \frac{\partial p}{\partial r} \right) = 0. \tag{2.36}$$

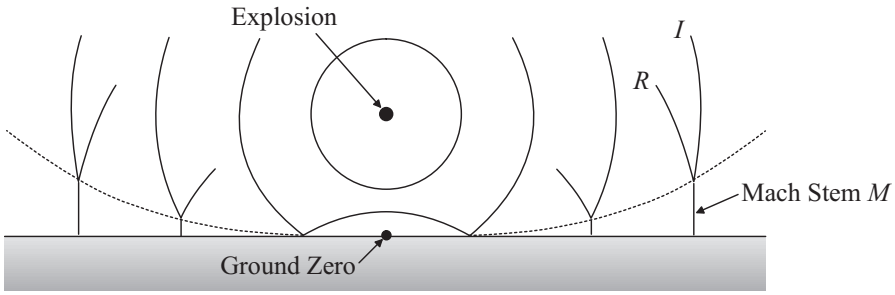


Figure 2.5: The Mach stem $M$ formed by an explosive shock is oriented perpendicular to the surface. The dotted line indicates the trajectory of the triple point, which is located at the intersection of the Mach stem, the incident shock $I$, and the reflected shock $R$. The point on the surface directly beneath the explosion is often called *ground zero*.

The general solutions that satisfy the spherical wave equation are of the form

$$p(r,t) = \frac{1}{r}F(r-ct) + \frac{1}{r}G(r+ct), \tag{2.37}$$

where $F$ and $G$ are arbitrary functions. From equation (2.37) it can be concluded that sound waves travel at a constant speed $c$ (hence the name speed of sound), and that the pressure attenuation of the sound wave is proportional to the inverse distance $1/r$.

### 2.2.3 Reflected Shock

When the shockwave impinges on a relatively unyielding surface, it undergoes a reflection into the opposite direction. The properties of the reflected shock are however different from the incident shock, because both shocks travel through media with different properties. Under most circumstances the shock is reflected, but when the shock impinges with enough velocity on a surface at near grazing incidence, something interesting occurs. Rather than being reflected, the shock is deflected, and the shock front spurts along over the surface. The result is a shock front that is oriented perpendicular to the surface, which is called a *Mach stem*. As can be seen in figure 2.5, the Mach stem begins to form at a certain distance away from ground zero, after which it steadily grows until the reflected shock has merged completely with the incident shock.

Figure 2.6 shows a detailed image of the region around the Mach stem in a shock–fixed coordinate system. As can be seen in the figure, the region around the Mach stem can be divided into four distinct regions, each with their own velocity. In this case the Mach number of the incident shock is given by:

$$M_{1,2} = \left(\frac{v_1}{c_1}\right)\sin\beta, \tag{2.38}$$

where $c_1$ is the speed of sound in region 1, and $\beta$ the angle of incidence as shown in figure 2.6. The Mach number of the Mach stem is given by $v_1/c_1$, since it also travels into the same medium as the incident shock. When this is combined with the previous

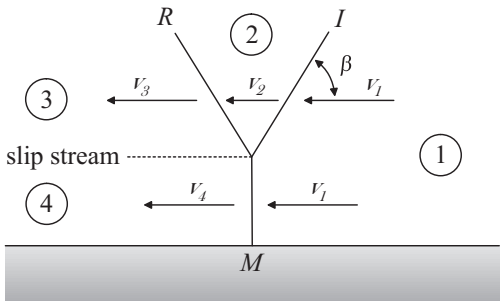


Figure 2.6: Detailed image of a Mach stem $M$ in a shock–fixed coordinate system. The incident and the reflected shock are indicated by $I$ and $R$ respectively. The dotted line represents the slip stream, which separates the flows in region 3 and 4.

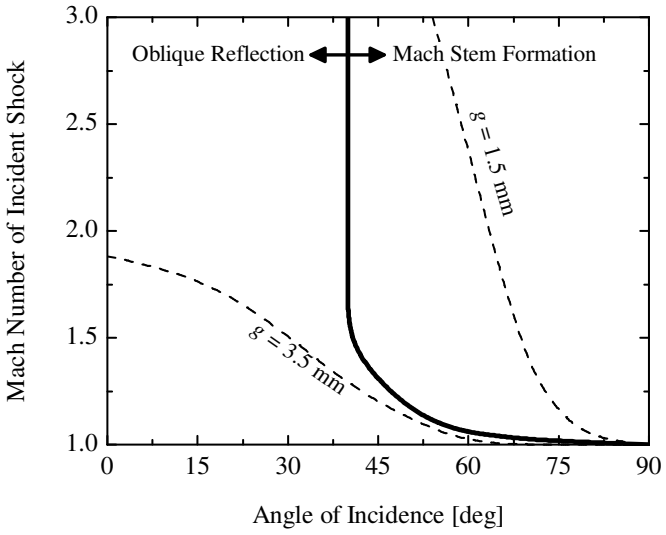


Figure 2.7: This chart shows where the transistion from oblique reflection into Mach stem formation takes place. The dotted lines in the graph show two possible paths through the parameter space. These paths were calculated for a shockwave energy of 115 mJ and a gap distance of 1.5 and 3.5 mm. Here it is clear that a gap distance of 1.5 mm leads to the formation of a Mach stem, and that a gap distance of 3.5 mm does not. (Source: Explosive Shocks in Air, G.F Kinney [12])

equation, it is possible to find the following expression for the Mach number of the Mach stem:

$$M_{1,4} = \frac{M_{1,2}}{\sin \beta}. \tag{2.39}$$

This result is very interesting, since it shows that the Mach stem has a higher Mach number than the incident shock. According to equation (2.23) this results in an increased pressure jump across the Mach stem, which should have a positive effect on the cleaning performance of the LSC method. Other characteristics that improve cleaning are the perpendicular orientation of the Mach stem, and the direction in which it travels. Unfortunately, a Mach stem only forms under specific conditions, which are summarized in figure 2.7. This chart shows that even for very strong shocks, there is no possibility of Mach stem formation when the angle of incidence has a value below 40°. Therefore, there is always an area underneath a point explosion in which Mach stem formation is not possible.

To put the effect of the Mach stem into perspective, consider the following example. Suppose that the shockwave energy released during LSC is equal to 100 mJ, and that the focal point is located 1 mm above the surface. The Mach number of the resulting shockwave at a distance of 3 mm from ground zero is then equal to 2.04, and the angle of incidence has a value of 72°. According to figure 2.7, this is well within the criteria for Mach stem formation. The Mach number of the Mach stem can be calculated with equation (2.39), and was found to be equal to 2.15. Inserting both Mach numbers into shock relation (2.23) shows that in this example the pressure jump across the Mach stem is 15% higher than the pressure jump across the incident shock.

# 3 Time Resolved Imaging of Laser Induced Breakdown

In this chapter the transient behavior of the shockwave generated by LIB is investigated. The shockwave was imaged with specialized techniques called *shadowgraphy* and *Schlieren photography*. The recorded images showed that the expansion of the shockwave was consistent with the Taylor & Sedov model for point explosions. Not only the expansion velocity, but also the shape of the shockwave was examined. It was found that the shape of the shockwave is ellipsoidal in the near field, and that it expands spherically in the far field. In addition to the shockwave, the images also revealed the formation of a Mach stem, and the hot air core produced by the LIB.

## 3.1 Flow Visualization

When working with transparent media, it is necessary to use a specialized technique to visualize the shockwaves traveling through the medium. In this chapter two closely related visualization techniques called *shadowgraphy* and *Schlieren photography* were used to make time resolved images of the LIB in air. These two techniques have in common that they are based on the deflection of light due to refractive index gradients in the medium. Therefore, the next subsection will first discuss the propagation of light in an inhomogeneous medium. The following two subsections will then discuss the shadowgraphy and Schlieren methods in more detail.

### 3.1.1 Light Propagation in Inhomogeneous Media

Light traveling through a region with refractive index gradients does not follow a straight line. According to *Fermat's principle*, light will always take the route with the shortest optical path length. The first order variation of the optical path length along the beam path must therefore vanish:

$$\delta \int n\left(x(s), y(s), z(s)\right)\, \mathrm{d}s = 0, \tag{3.1}$$

where $n(x, y, z)$ is the refractive index field and $\mathrm{d}s$ is an infinitesimal displacement along the beam path. The solution to this variational problem must satisfy the corresponding system of Euler–Lagrange equations:

$$\frac{d}{ds}\left(n\frac{dx}{ds}\right) = \frac{\partial n}{\partial x}, \tag{3.2}$$

$$\frac{d}{ds}\left(n\frac{dy}{ds}\right) = \frac{\partial n}{\partial y}, \tag{3.3}$$

$$\frac{d}{ds}\left(n\frac{dz}{ds}\right) = \frac{\partial n}{\partial z}. \tag{3.4}$$

When the problem is restricted to beam paths which always have a component in the $z$–direction, it is possible to describe the beam path by $x = x(z)$ and $y = y(z)$. This is

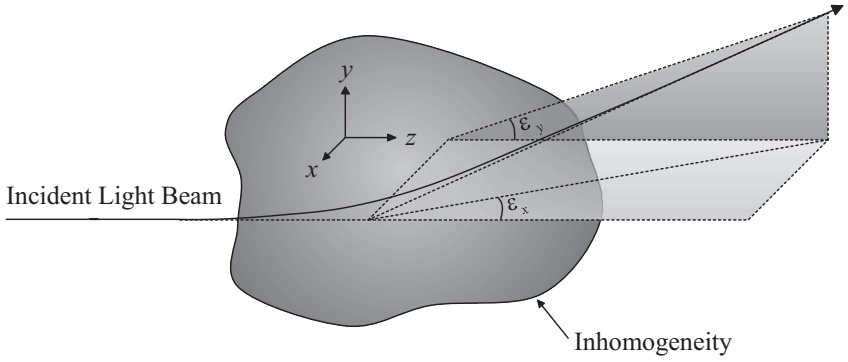


Figure 3.1: Deflection of a light beam by the refractive index gradients within a transparant medium. The incident light beam initially travels along the $z$–axis before it is deflected over the angles $\epsilon_x$ and $\epsilon_y$ by the inhomogeneity.

not a very harsh restriction, but it merely ensures that the light beam is able to cross the inhomogeneity. After a rather lengthy and tedious algebraic calculation equations (3.2)–(3.4) can be rewritten into:

$$\frac{d^2x}{dz^2} = \left\{1+\left(\frac{dx}{dz}\right)^2+\left(\frac{dy}{dz}\right)^2\right\}\left\{\frac{1}{n}\frac{\partial n}{\partial x}-\frac{dx}{dz}\frac{1}{n}\frac{\partial n}{\partial z}\right\}, \tag{3.5}$$

$$\frac{d^2y}{dz^2} = \left\{1+\left(\frac{dx}{dz}\right)^2+\left(\frac{dy}{dz}\right)^2\right\}\left\{\frac{1}{n}\frac{\partial n}{\partial y}-\frac{dy}{dz}\frac{1}{n}\frac{\partial n}{\partial z}\right\}. \tag{3.6}$$

This system of differential equations can be simplified considerably, by assuming that the slope of the light beam and the refractive index gradient are much smaller than unity. Equations (3.5) and (3.6) are then reduced to:

$$\frac{d^2x}{dz^2} = \frac{1}{n}\frac{\partial n}{\partial x}, \tag{3.7}$$

$$\frac{d^2y}{dz^2} = \frac{1}{n}\frac{\partial n}{\partial y}. \tag{3.8}$$

This effectively decouples both differential equations, and the deflection angles (see figure 3.1) of a light beam passing through the refractive index field can now be calculated by integrating equations (3.7) and (3.8):

$$\epsilon_x = \int_{z_1}^{z_2}\frac{1}{n}\frac{\partial n}{\partial x}\,\mathrm{d}z, \tag{3.9}$$

$$\epsilon_y = \int_{z_1}^{z_2}\frac{1}{n}\frac{\partial n}{\partial y}\,\mathrm{d}z, \tag{3.10}$$

where $z_1$ and $z_2$ mark the beginning and end of the inhomogeneity. For a two-dimensional inhomogeneity of extent $L$ these two equations can be further reduced to:

$$\epsilon_x = \frac{L}{n}\frac{\partial n}{\partial x}, \tag{3.11}$$

$$\epsilon_y = \frac{L}{n}\frac{\partial n}{\partial y}. \tag{3.12}$$

| Wavelength [nm] | $K$ [cm$^3$/kg] |
|---|---|
| 356.2 | 0.2330 |
| 407.9 | 0.2304 |
| 509.7 | 0.2274 |
| 607.4 | 0.2259 |
| 703.4 | 0.2250 |
| 912.5 | 0.2239 |

Table 3.1: Gladstone–Dale constants of air at $T = 288$ K. (Source: Flow Visualization, W. Merzkirch [14])

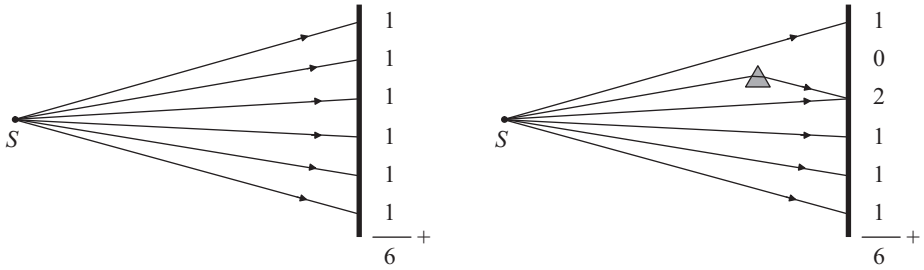


Figure 3.2: Simple setup for a shadowgraphy experiment, consisting of a point light source ($S$) and a screen. (a) When there are no inhomogeneities present, the light will travel in a straight line from the point light source to the screen. (b) The introduction of an inhomogeneity in one of the beam paths causes a deflection of the light beam. As a consequence, the light is redistributed over the screen.

These two equations show that the deflection angle is directly proportional to the refractive index gradient. With the help of the *Gladstone–Dale* relation [14] it is possible to rewrite the refractive index gradients into density gradients:

$$n - 1 = K\rho, \tag{3.13}$$

where $n$ is the refractive index, $\rho$ the density, and $K$ the Gladstone–Dale constant. Table 3.1 shows a listing of Gladstone–Dale constants for a range of wavelengths. Inserting the Gladstone–Dale relation into equations (3.11) and (3.12) clearly shows that the deflection angles $\epsilon_x$ and $\epsilon_y$ are also directly proportional to the density gradient:

$$\epsilon_x = \frac{KL}{1 + K\rho}\left(\frac{\partial \rho}{\partial x}\right), \tag{3.14}$$

$$\epsilon_y = \frac{KL}{1 + K\rho}\left(\frac{\partial \rho}{\partial y}\right). \tag{3.15}$$

### 3.1.2 Shadowgraphy

One of the simplest methods to visualize density gradients in transparent media is shadowgraphy. The principle of this technique is illustrated by figure 3.2, which shows how light from a single point light source is deflected by a density gradient in its beam path. As a

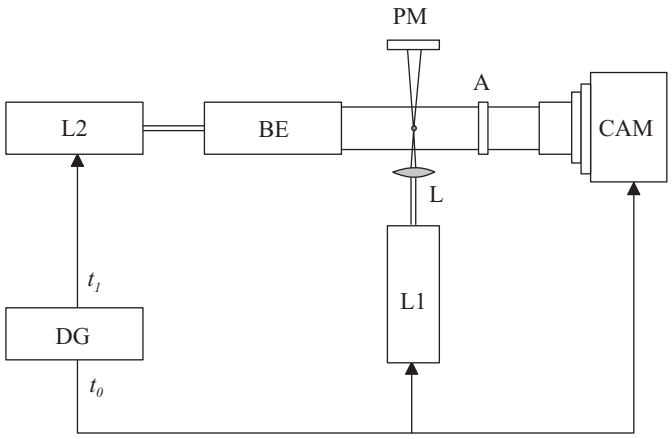


Figure 3.3: Schematic sketch of the laser flash shadowgraphy setup. (L1) Nd:YAG Laser (LIB). (L2) Nd:YLF Laser (Imaging). (BE) Beam Expander. (A) Attenuator. (CAM) CCD Camera. (L) Plano–Convex Lens. (DG) Delay Generator. (PM) Power Meter.

result some parts of the screen are less illuminated while other parts are more illuminated. The resulting image with lighter and darker regions is called a shadowgraph. Although shadowgraphy is one of the simplest methods available, it is also one of the least sensitive. Shadowgraphy is only sensitive to the second derivative of the density. This means that this method is not very well suited for the visualization of detailed structures, but it is ideally suited for the visualization of shockwaves.

A shadowgraphy setup contains two essential components: a light source, and a screen or recording device. The light source that was used for the imaging experiments presented in this thesis, is a frequency doubled Q-switched Nd:YLF laser made by New Wave Research. It has a wavelength of 527 nm, and a FWHM pulse width of 100 ns, which is short enough to capture the moving shockwave. The LIB was produced with a Q-switched Nd:YAG laser, which has a wavelength of 1064 nm, a pulse width of 10 ns, and a maximum pulse energy of 350 mJ. The light from the Nd:YAG laser was focused with a single plano–convex $CaF_2$ lens. The beam from the illumination laser is expanded by a beam expander to create a collimated beam with a diameter of 40 mm. The LIB is created in the center of the collimated beam, and was recorded with a standard industrial CCD camera (Foculus FO432C). A digital delay generator (DG535, Stanford Research Systems) was used for the correct timing of both laser triggers and the camera trigger. Figure 3.3 shows a schematic sketch of the laser flash shadowgraphy setup.

As mentioned before, shadowgraphy is only sensitive to changes in the second derivative of the density. To demonstrate the sensitivity of this shadowgraphy setup, consider a transparent plate of a homogeneous material and constant thickness, as illustrated in figure 3.4a. The light that enters from the left is not affected by the constant density field and will traverse the plate undisturbed. The screen located at the right of the plate is uniformly illuminated. In figure 3.4b the plate has been replaced by a wedge with flat surfaces. In this case the first derivative of the density is constant. Light entering from the left is now deflected by a constant angle, and the screen on the right is still uniformly illuminated. Replacing one flat surface of the wedge with a curved surface results in a density field with a constant second derivative. The wedge converges the light, as can be seen in figure 3.4c. This results in a more intense, but still uniform, illumination of the

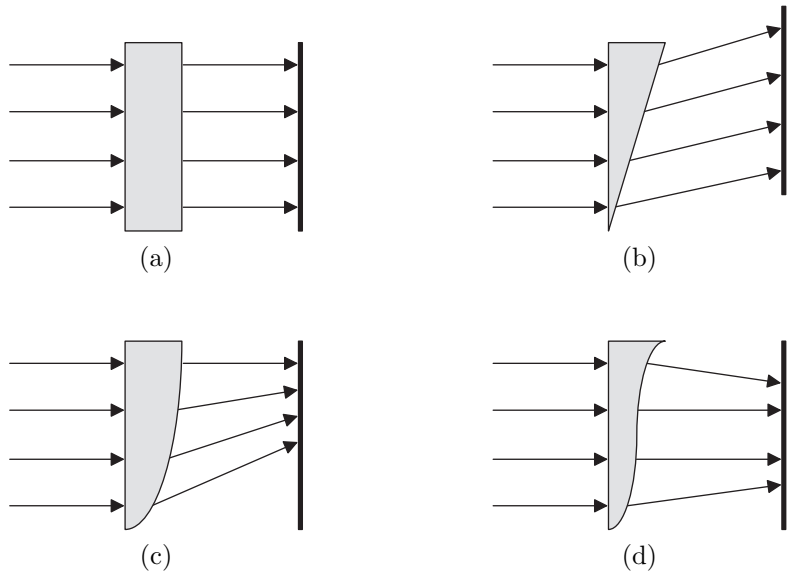


Figure 3.4: Deflection of a collimated light beam passing through a density field with a (a) constant value, (b) constant derivative, (c) constant second derivative, and (d) variable second derivative.

screen. To achieve non-uniform illumination of the screen, the second derivative of the density has to be nonzero. Only then will it be possible to derive information about the density distribution from the image on the screen. Figure 3.4d shows an arrangement in which this is the case. From this it can be concluded that a shadowgraph is only sensitive to changes in the second derivative of the density.

A more formal definition of the sensitivity is given by Settles [15]:

$$S_x = \frac{\Delta I}{I_0} = g\left(\frac{\partial \epsilon_x}{\partial x}\right), \qquad S_y = \frac{\Delta I}{I_0} = g\left(\frac{\partial \epsilon_y}{\partial y}\right), \tag{3.16}$$

where $I_0$ is the intensity of the light, $\Delta I$ the change in intensity, and $g$ the distance between the inhomogeneity and the screen. The deflection angles $\epsilon_x$ and $\epsilon_y$ are directly proportional to the first derivative of the density, as can be seen in equations (3.14) and (3.15). Shadowgraphy is therefore sensitive to the second derivative of the density.

### 3.1.3 Schlieren Photography

Schlieren photography is another visualization technique that can be used to visualize density gradients in transparent media. It is closely related to shadowgraphy, but there are also a couple of important differences. First of all, a Schlieren image is a properly focused image, while a shadowgraph is only a shadow. Second, Schlieren setups are generally more complicated, and need a knife edge or an other type of cutoff. Finally, Schlieren methods are more sensitive than shadowgraphy, which makes them more suitable for the visualization of fine details.

A Schlieren setup is more complicated than a shadowgraphy setup, as can be seen in figure 3.5. In this case the illumination is provided by a so–called Schlieren illuminator, which consists of a halogen light source, a condenser lens, and an adjustable slit. The condenser lens produces an intermediate image of the halogen light source, which is then

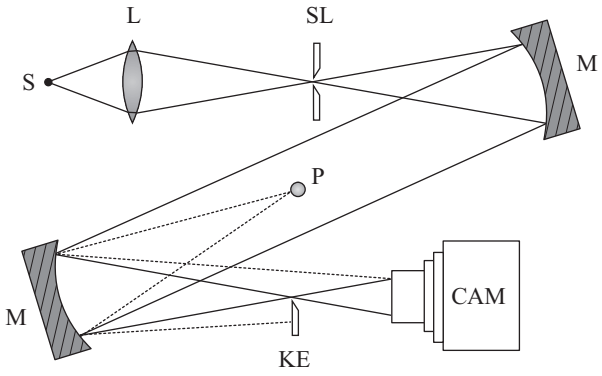


Figure 3.5: Schematic drawing of a Z–type Schlieren setup, whch is named after the shape of the letter Z. (S) Halogen Light Source. (L) Condenser Lens. (SL) Adjustable Slit. (M) Parabolic Mirror. (KE) Knife Edge. (CAM) Intensified CCD Camera. (P) Plasma.

cropped by the adjustable slit to produce an approximately uniform light source with well defined edges. After the light leaves the Schlieren illuminator, it is collimated and refocused by a set of parabolic mirrors. This produces a second intermediate image of the light source at the focal point of the second parabolic mirror. The knife edge at the focal point of the second parabolic mirror is mounted on a translation stage, and is oriented in the same direction as the slit of the Schlieren illuminator. The knife edge functions as a cutoff, that can be moved into and out of the focal point, to block (a part of) the light source image before it reaches the camera. On the other hand, light that is deflected by an inhomogeneity will either be blocked, or pass the cutoff plane undisturbed. This depends on the sign of the density gradient that deflected the light, as is illustrated by the dashed lines in figure 3.5. The resulting image shows brighter and darker regions, which are a measure of the size and sign of the first derivative of the density. In other words, Schlieren methods are sensitive to the first derivative of the density, as is evident from the following expression for the sensitivity [15]:

$$S_x = \frac{\Delta I}{I_0} = \frac{f\epsilon_x}{a}, \qquad S_y = \frac{\Delta I}{I_0} = \frac{f\epsilon_y}{a}, \tag{3.17}$$

where $I_0$ is the intensity of the light, $\Delta I$ the change in intensity, $f$ the focal distance of the second parabolic mirror, and $a$ is equal to the width of the unobstructed part of the intermediate light source image at the knife cutoff. Here $a = 0$ corresponds to the situation in which the intermediate light source image is completely blocked by the knife edge. According to equation (3.17) this will result in an infinitely high sensitivity. In practice however, this is never achieved because diffraction effects will limit the sensitivity. Since the deflection angles $\epsilon_x$ and $\epsilon_y$ are given by equation (3.14) and (3.15), the sensitivity is indeed proportional to the first derivative of the density. Schlieren methods are therefore more suitable for the visualization of fine details than shadowgraphy, because the sensitivity of shadowgraphy is proportional to the second derivative of the density (see equation (3.16)).

The Z-type Schlieren setup described in the previous paragraph was used to make time resolved images of the LIB process. The LIB was created with a Nd:YAG laser, which has a wavelength of 1064 nm, and a pulse length of 10 ns. The laser light was focused with

a single plano–convex $CaF_2$ lens between the two 108 mm f/8 parabolic mirrors. The camera that was used for this setup was an intensified CCD camera (Stanford Computer Optics), which is capable of very short exposure times below 10 ns. The correct timing of the Nd:YAG laser and the iCCD camera was taken care off by a digital delay generator (DG535, Stanford Research Systems).

## 3.2 Time Resolved Images

With the help of the shadowgraphy and Schlieren setups described in the previous section, it was possible to make time resolved images of the LIB in air. Both visualization techniques were used in the following subsections to investigate the behavior of the shockwave in the near and far field. Furthermore, it was also investigated what happens when the shockwave impinges on a flat surface, and what happens to the hot air core left by the LIB.

### 3.2.1 Behavior of the Shockwave in the Near Field

Figure 3.6 shows a selection of images that were made with the shadowgraphy setup described in section 3.1.2. These images show the evolution of the shockwave in air for different pulse energies and focal lengths at room temperature and atmospheric pressure. From the images, it can be concluded that the shape of the shockwave is not spherical but more ellipsoidal, especially in the beginning of the expansion. The reason for this nonspherical expansion can be found in the elongated shape of the plasma immediately after the laser pulse. The plasma is elongated because the initial shock front generated by the breakdown changes the air into an absorbing plasma, and the laser energy is absorbed directly behind the shock front [9]. This causes the shock front to propagate more strongly towards the lens during the laser pulse, resulting in an elongated plasma. In this case the shock relations derived in section 2.2.1 will have to be modified, to take the energy addition behind the shock front into account. The resulting theory is called the Chapman–Jouguet theory [11], and it can be used to calculate the propagation velocity along the optical axis during the laser pulse [16]:

$$v_{\mathrm{axi}} = \left[2\left(\gamma^2 - 1\right)\frac{\mu I}{\rho}\right]^{1/3}, \qquad [\mathrm{I}] = \mathrm{W/m^2}, \qquad [\rho] = \mathrm{kg/m^3} \tag{3.18}$$

where $I$ is the intensity of the laser beam at the shock front, $\rho$ the density, and $\mu$ the fraction of laser light that is absorbed directly behind the shock front. As a first approximation, the lateral expansion velocity, which is perpendicular to the axial velocity, is equal to the speed of sound in the plasma:

$$v_{\mathrm{lat}} = \sqrt{\frac{\gamma k_{\mathrm{b}} \bar{Z} T_{\mathrm{e}}}{M}}, \tag{3.19}$$

where $\gamma$ is the specific heat ratio, $k_{\mathrm{b}}$ Boltmann's constant, $\bar{Z}$ the average charge state, $T_{\mathrm{e}}$ the electron temperature, and $M$ the ion mass. With the help of the Chapman–Jouguet theory, the ratio of both velocities can be estimated with the following expression [16]:

$$\frac{v_{\mathrm{axi}}}{v_{\mathrm{lat}}} \approx \frac{1+\gamma}{\gamma}, \tag{3.20}$$

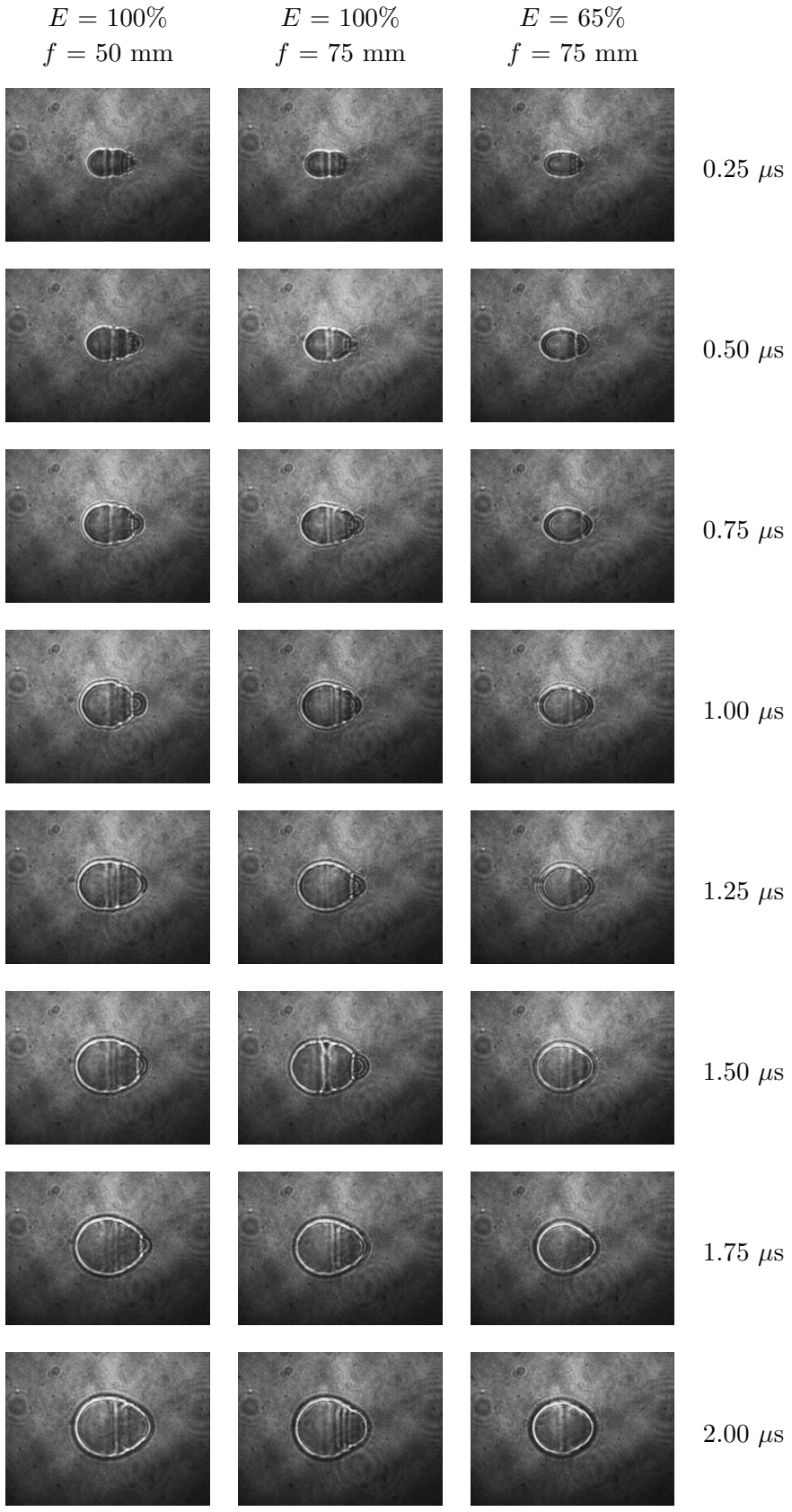


Figure 3.6: Time resolved shadowgraphs of LIB in air at atmospheric pressure and room temperature. The Nd:YAG laser and the focusing lens are located to the left of each image, and the dimensions of each image are $(19 \times 14)$ mm$^2$.

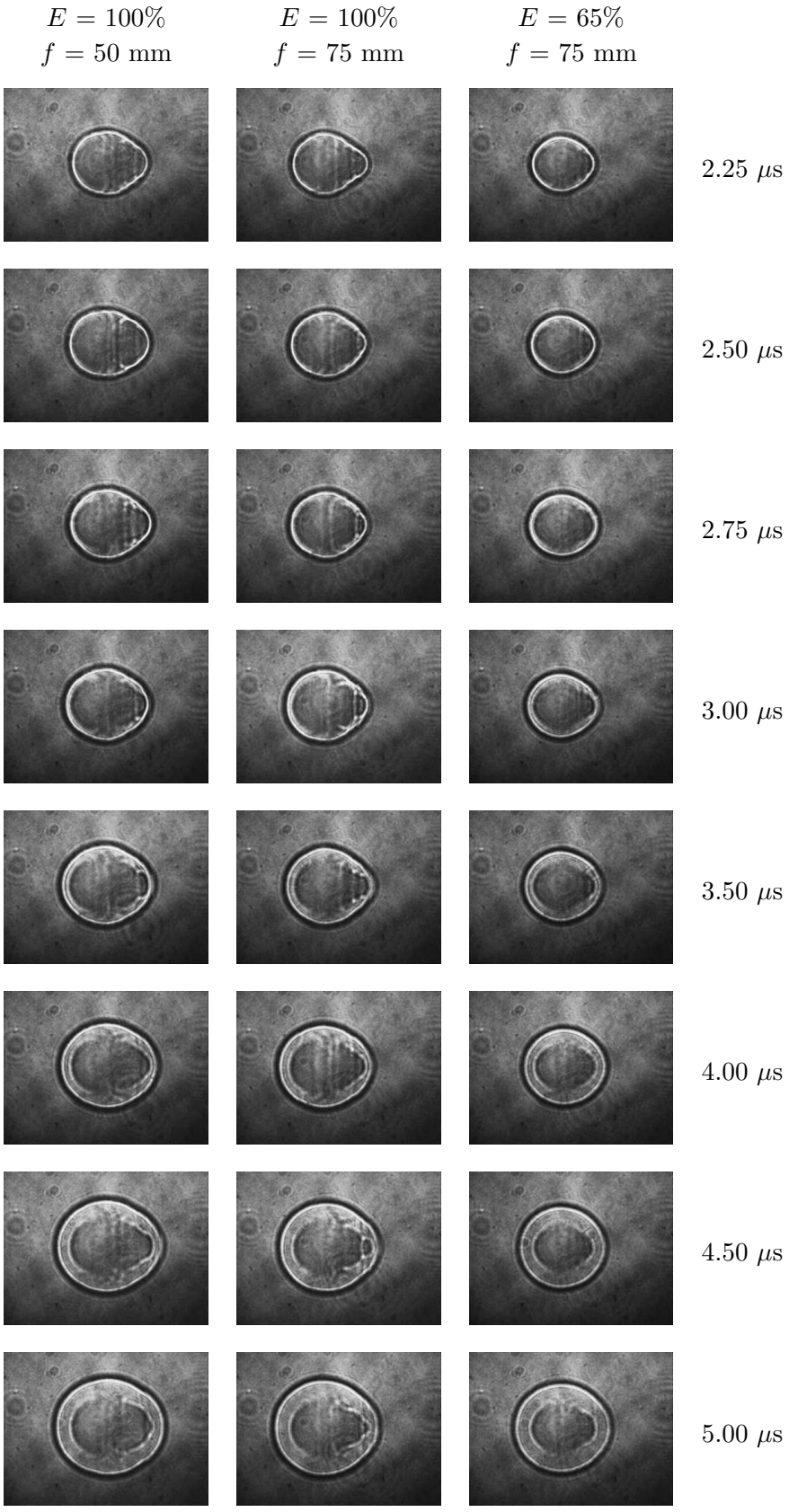


Figure 3.6: Time resolved shadowgraphs of LIB in air at atmospheric pressure and room temperature (continued). The Nd:YAG laser and the focusing lens are located to the left of each image, and the dimensions of each image are $(19 \times 14)$ mm$^2$.

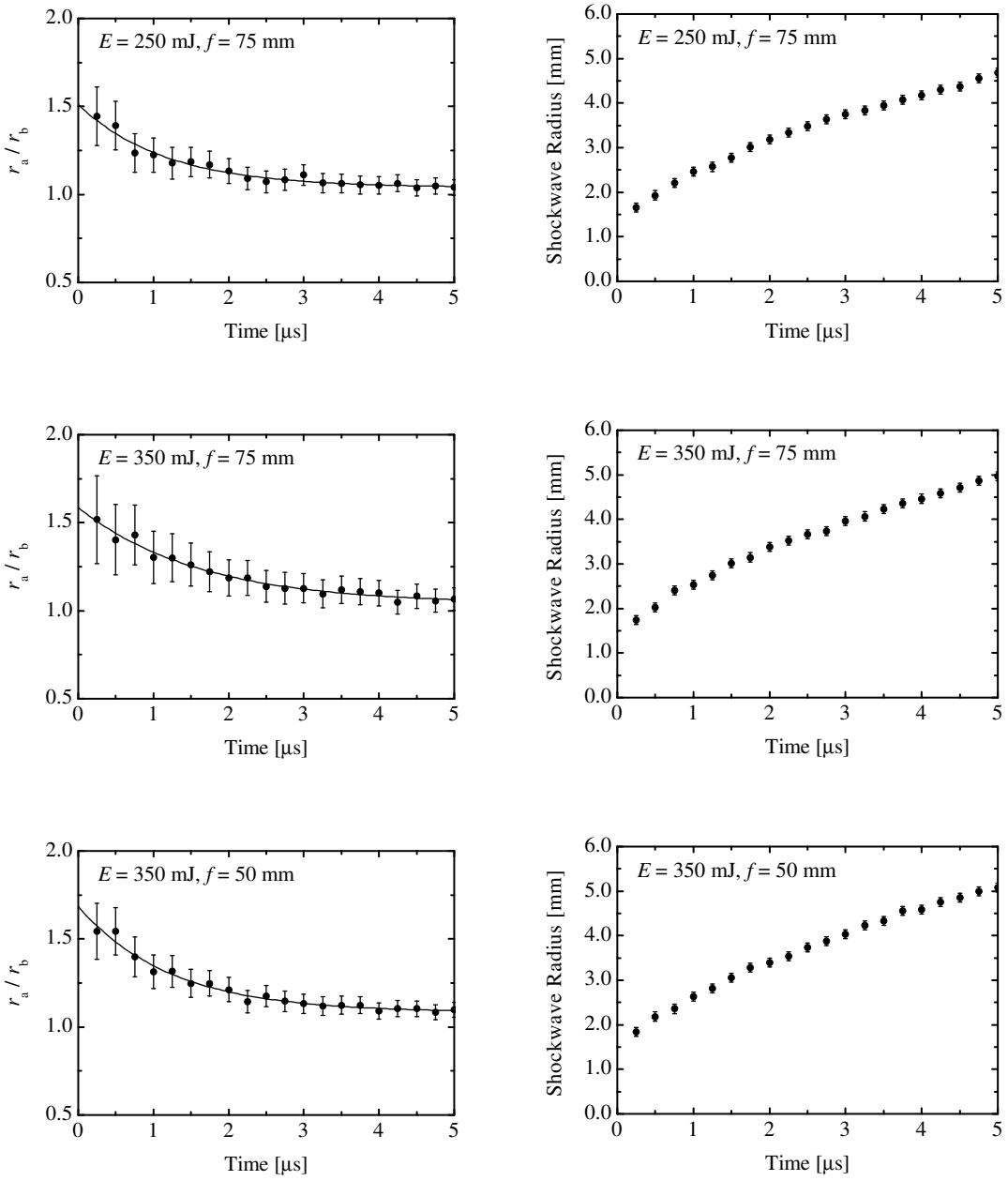


Figure 3.7: The left column shows how the ratio of the long and short axis of the ellipsoidal shockwave changes with time. The right column also shows the sphere equivalent radius of the shockwave.

| $E$ [mJ] | $f$ [mm] | $r_\mathrm{a}/r_\mathrm{b}$ | $\log r_\mathrm{s}/\log t$ | $W$ [mJ] | CE |
|---|---|---|---|---|---|
| 250 | 75 | $1.51 \pm 0.18$ | $0.38 \pm 0.01$ | $85 \pm 2$ | $0.34 \pm 0.01$ |
| 350 | 75 | $1.59 \pm 0.24$ | $0.39 \pm 0.01$ | $114 \pm 3$ | $0.33 \pm 0.01$ |
| 350 | 50 | $1.68 \pm 0.17$ | $0.39 \pm 0.01$ | $130 \pm 4$ | $0.37 \pm 0.02$ |

Table 3.2: Summary of the most important shockwave characteristics for two different pulse energies $E$ and focal lengths $f$. The table also lists the the conversion effciciency CE, which is defined as the ratio between the energy of the shockwave and the energy of the laser pulse.

which yields 1.71 for air ($\gamma = 1.40$). The same type of relationship must also apply to the ratio of the axial and lateral dimensions of the plasma during the laser pulse. This was confirmed by figure 3.7, which shows the ratio of the long and short axis for different pulse energies and focal lengths. Fitting and extrapolating this data with an exponentially decaying function yields values which are indeed approximately equal to the value found with equation (3.20). These values are summarized in table 3.2.

Because the shockwave is not spherical, it is not possible to use equation (2.27) directly. Fortunately, the Taylor & Sedov solution can be modified to include elliptically expanding shockwaves, by replacing the radius $r_\mathrm{s}$ with the radius of a sphere that has the same volume as the ellipsoid [17]:

$$r_s = \left(r_\mathrm{a} r_\mathrm{b}^2\right)^{1/3}, \tag{3.21}$$

where $r_\mathrm{a}$ is the long semi axis, and $r_\mathrm{b}$ the short semi axis of the ellipsoid. The graphs in figure 3.7 show how the sphere equivalent shockwave radius $r_\mathrm{s}$ changes with time for different pulse energies and focal lengths. From these graphs it can be concluded that the expansion velocity increases for higher pulse energies and smaller focal lengths. Plotting $t^2$ versus $r_s^5$ results in a straight line, as can be seen in the right column of figure 3.8. According to equation (2.27) the slope of this line can be used to calculate the energy of the shockwave in the following way:

$$W = \frac{\rho a}{Y^5(\gamma)}, \tag{3.22}$$

where $a$ is the slope of the line, $\rho$ the density of the air, and $Y$ the empirical Taylor & Sedov coefficient listed in table 2.1. Table 3.2 shows the measured shockwave energies, as well as their respective conversion efficiencies. These conversion efficiencies show which portion of the laser light is converted into shockwave energy, and they are defined as follows:

$$\mathrm{CE} = \frac{E}{W} \tag{3.23}$$

where $E$ is the energy of the laser pulse, and $W$ the energy associated with the shockwave. Table 3.2 shows that the conversion efficiency is higher for smaller focal lengths, which explains why the lens with the shorter focal length produces a higher expansion velocity for the same pulse energy. These results are in agreement with Mori [17], who found a conversion efficiency of 0.40 in air at atmospheric pressure. Figure 3.8 also shows a collection of log–log plots of the measured shockwave radius versus the time. As can be seen in table 3.2, these plots yielded slopes which were consistent with the expected theoretical value of 0.40. This result, and the other results presented here, confirm that the shockwave can be described with the Taylor & Sedov model in the near field.

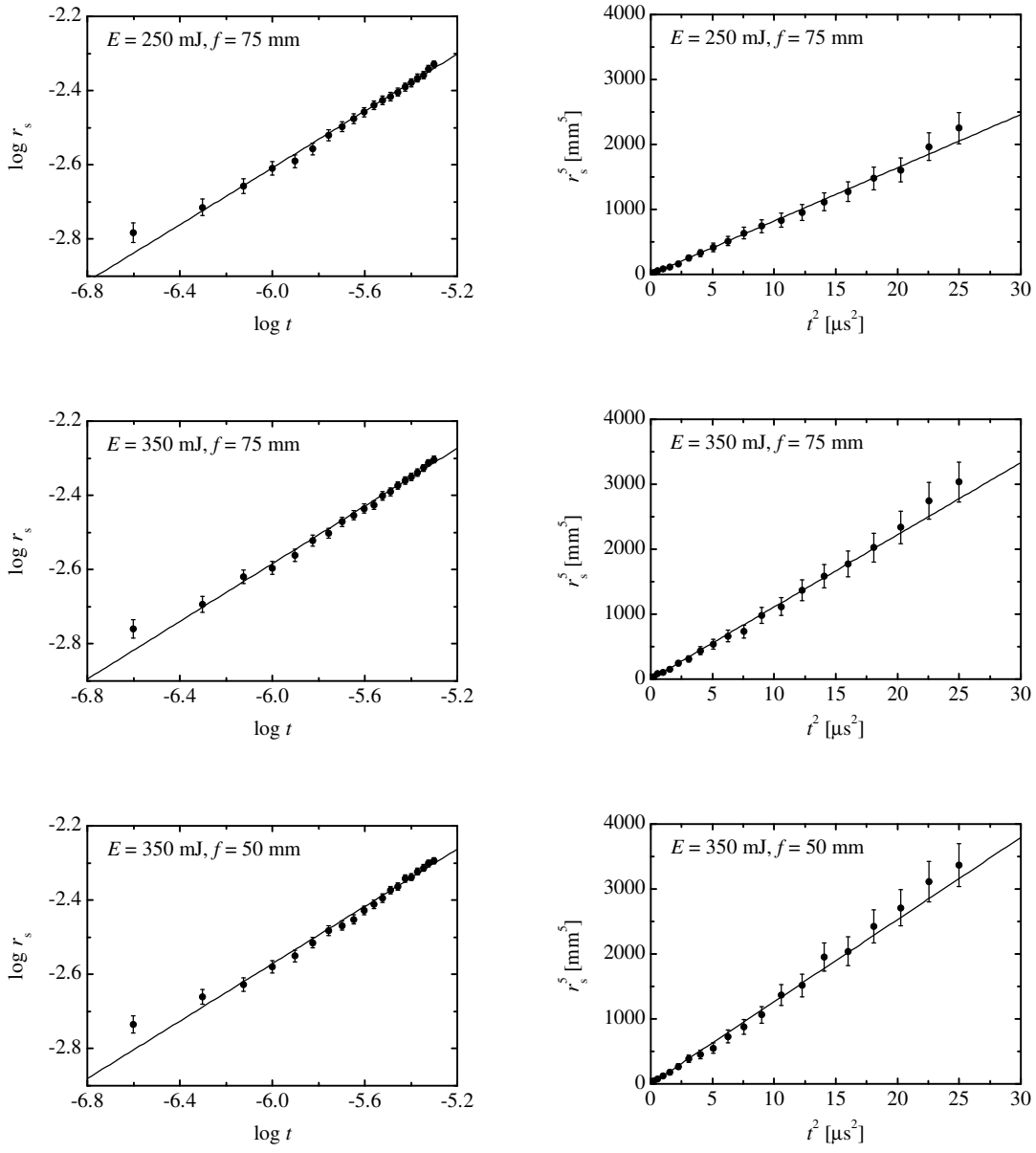


Figure 3.8: The left column shows a collection of log–log plots of the shockwave radius versus the time, and the plots in the right column show the relationship between $t^2$ and $r_{\mathrm{s}}^5$.

### 3.2.2 Behavior of the Shockwave in the Far Field

In section 3.2.1 it was established that in the near field the shockwave behaves as predicted by the Taylor & Sedov theory [13]. This section will further investigate the behavior of the shockwave in the far field, where the shockwave has slowed down considerably and approaches the speed of sound. This was done with the Schlieren setup described in section 3.1.3. Figure 3.9 shows a collection of Schlieren photographs that were taken (5–100) $\mu$s after the beginning of the laser pulse. These images show that the shockwave has lost its elliptical shape somewhere between 5 and 10 $\mu$s, and that it expands spherically in the far field. Plotting the shockwave radius as a function of time results in a straight line with a slope of $(367 \pm 3)$ ms$^{-1}$, as can be seen in figure 3.10. This velocity is only slightly above the speed of sound, which confirms that the shockwave eventually degenerates into a normal sound wave.

### 3.2.3 Reflected Shockwaves and Mach Stem Formation

The time resolved images presented in the previous two subsections show how the shockwave evolves when it is not obstructed by a surface or any other object. But during LSC the laser beam is focused a small distance above the surface, which leads to reflection of the shockwave and possibly Mach stem formation. This can be seen in figure 3.11 and 3.12, which show the interaction of the shockwave with a flat surface for two different gap distances and a laser pulse energy of 350 mJ. The first figure shows the reflection of the shockwave and the formation of a Mach stem for a gap distance of 1.5 mm. The second figure shows the behavior of the shockwave when the gap distance is increased to 3.5 mm. In this case the shockwave undergoes a reflection, but there is no Mach stem formation. This can be understood by looking at the dashed lines in figure 2.7. At a gap distance of 3.5 m the shockwave has already slowed down too much before it reaches the critical angle of incidence of 40°, and is therefore unable to cross the boundary that separates the two regimes of Mach stem formation and oblique reflection.

### 3.2.4 Evolution of the Hot Air Core

The previous sections were concerned with the behavior of the shockwave in the near and far field. For completeness, this section will very briefly investigate the behavior of the hot air core left by the LIB. This was done with the same Schlieren setup that was used in the previous section, and the recorded images can be found in figure 3.13. These images show that the LIB produces a very turbulent hot air core, which expands with a velocity well below the speed of sound. For instance, the average velocity of the plume of hot air that is ejected from the main body is approximately equal to 10 ms$^{-1}$, which is indeed much smaller than the speed of sound.

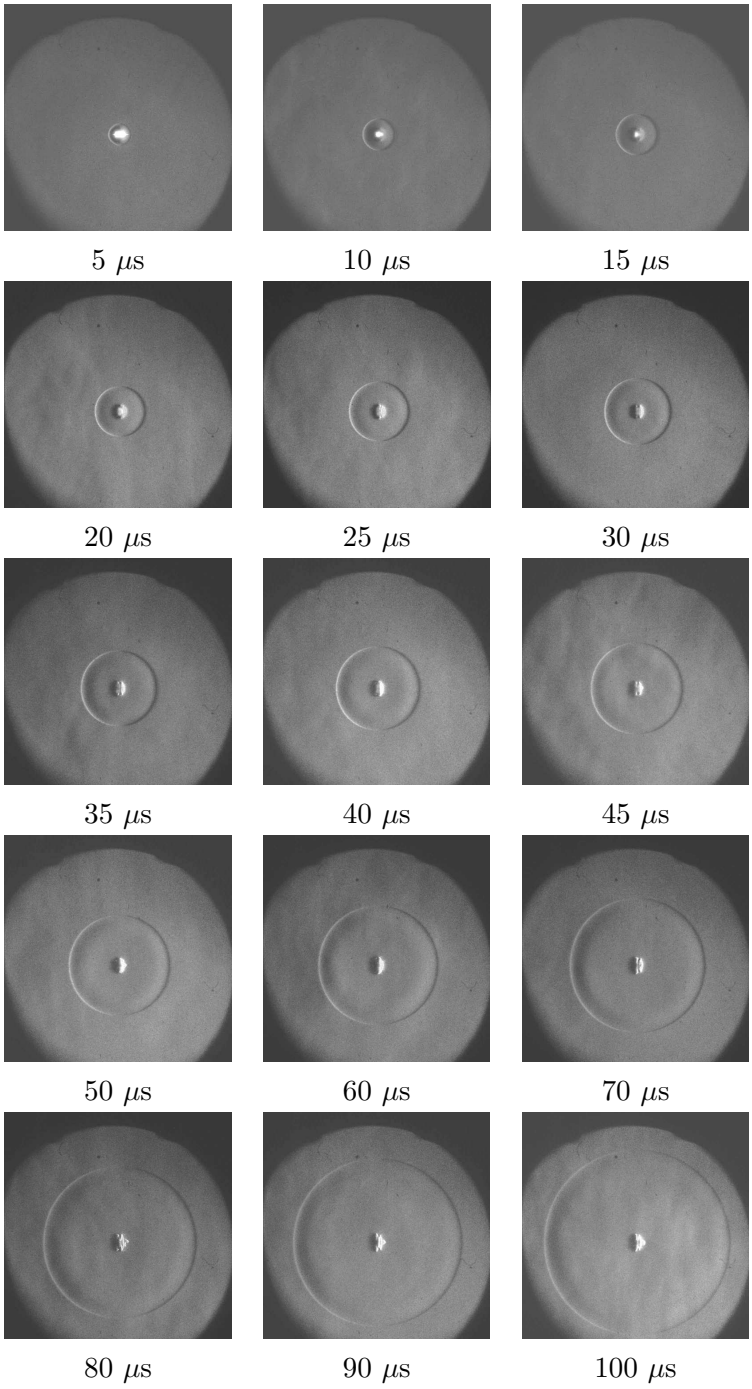


Figure 3.9: Time resolved Schlieren photographs of the shockwave produced by the LIB in air at atmospheric pressure and room temperature. The expanding ring is the shockwave generated by the LIB. The focusing lens was situated to the right of each image, and has a focal length 75 mm. The energy of the laser pulse was set to 350 mJ, and the images are $(90 \times 90)$ mm$^2$ in size.

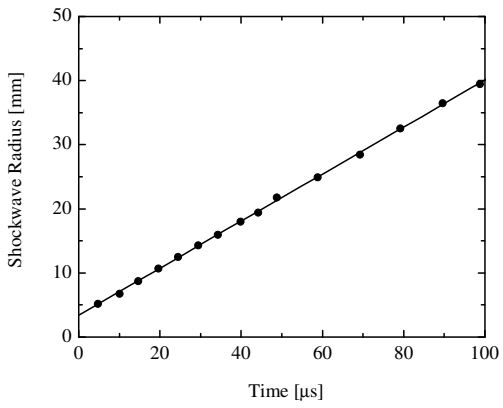


Figure 3.10: Shockwave radius as a function of time in the far field for a laser pulse energy of 350 mJ and a focal length of 75 mm. The linear fit corresponds to a velocity of (367 ± 3) $ms^{-1}$.

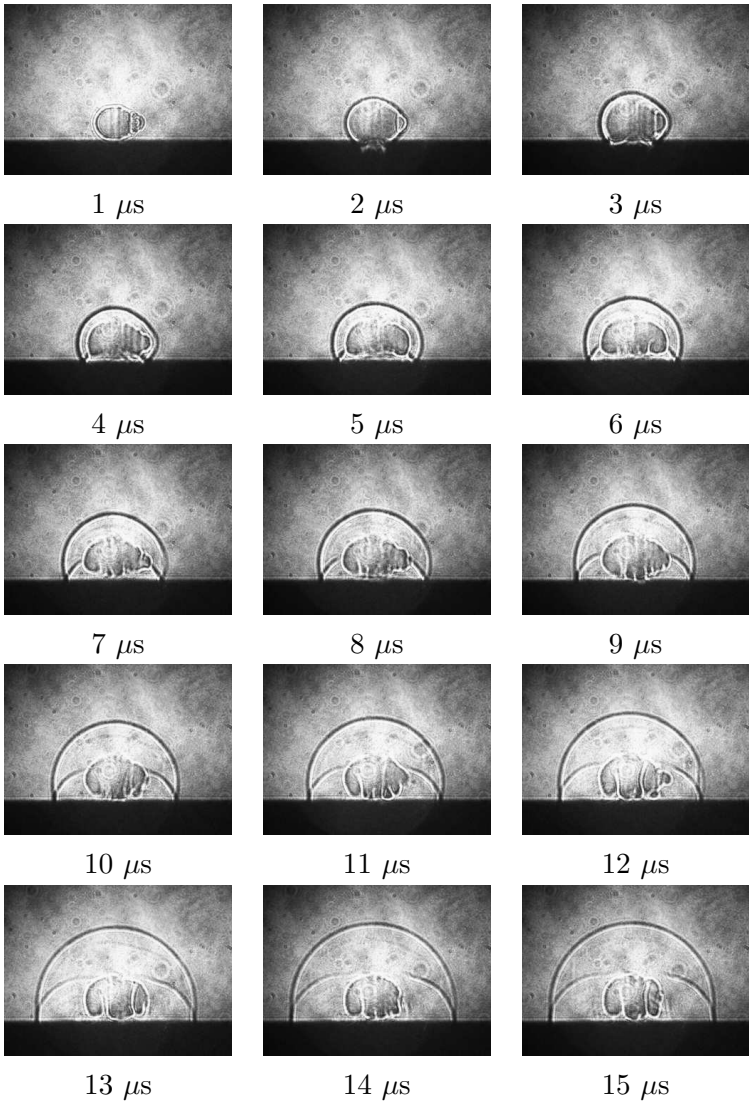


Figure 3.11: Shadowgraphs showing the formation of a Mach stem as a result of LIB at a distance of 1.5 mm above the surface. The focusing lens and Nd:YAG laser are situated to the left of each image, and the images are $(17 \times 13)$ mm$^2$ in size.

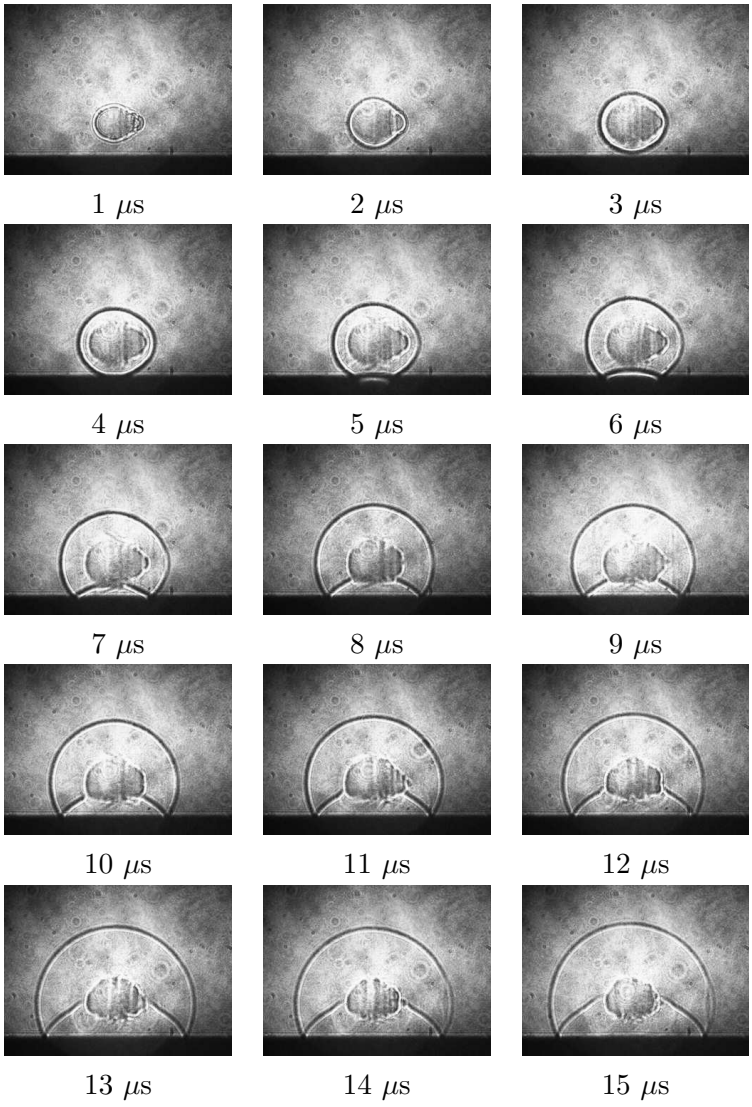


Figure 3.12: Shadowgraphs showing the reflection of a shockwave generated by the LIB at a distance of 3.5 mm above the surface. The focusing lens and Nd:YAG laser are situated to the left of each image, and the images are $(17 \times 13)$ mm$^2$ in size.

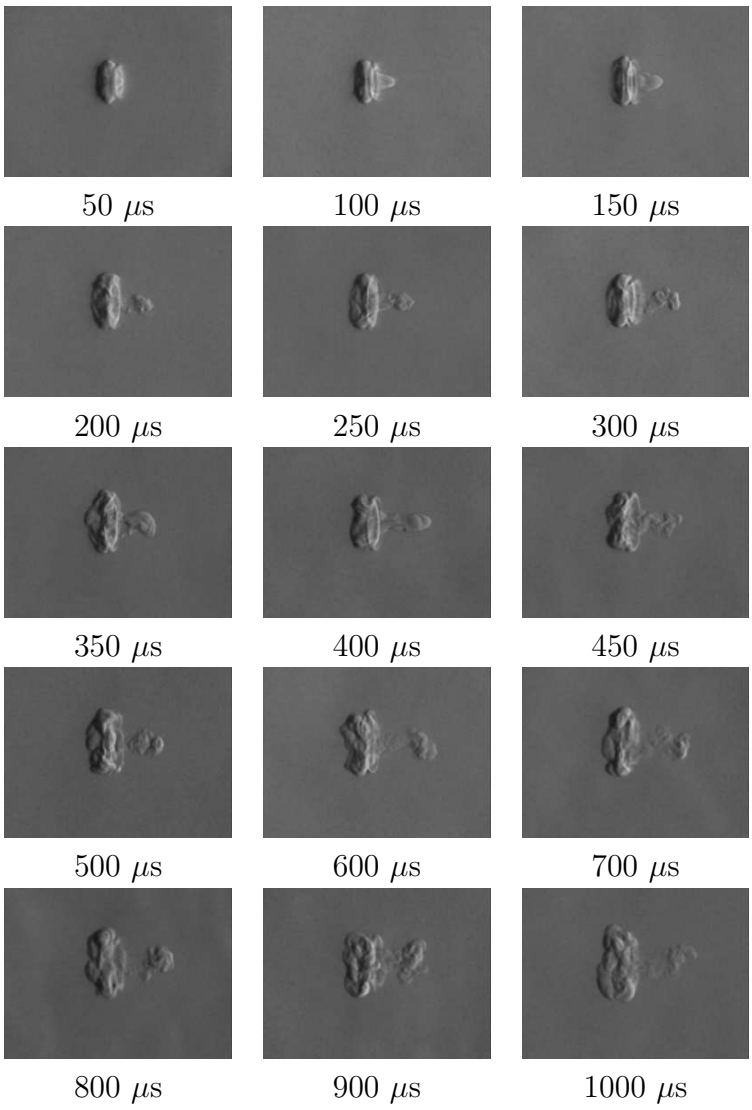


Figure 3.13: Time resolved Schlieren photographs of the hot air core produced by the LIB in air at atmospheric pressure and room temperature. Again, the focusing lens is situated to the right of the image, and the images are $(29 \times 20)$ mm$^2$ in size.

# 4 Theory of Adhesion

In this chapter the theoretical background of adhesion will be explored. It is found that the adhesion forces at the interface between two macroscopic bodies are caused by electromagnetic interactions at the molecular level. As will be shown in this chapter, the two most important adhesion forces for sub–micrometer particles are the capillary force and the van der Waals force. At the end of this chapter a model is presented in which the adhesion theory and the gas dynamics theory from chapter 2 are used to predict the cleaning performance of the LSC method.

## 4.1 Origin of Adhesion Forces

It is now commonly accepted that every phenomenon observed in nature can be explained by one of the four fundamental forces of nature. These forces are the strong and weak interactions, the electromagnetic force, and the gravitational force. The intermolecular forces that lead to the adhesion of small particles to a surface, must therefore originate from one of these four fundamental forces.

The strong and weak interactions are used to describe the interactions between neutrons, protons and other elementary particles. Their range of interaction is much shorter than the typical intermolecular distance. Therefore, these two forces cannot be the source of the adhesion forces between two macroscopic bodies. The gravitational and electromagnetic forces have a much larger range of interaction, which ranges from subatomic distances to infinity. But the gravitational forces lack the necessary repulsive component to accurately describe intermolecular interactions. In contrast to the gravitational forces, the electromagnetic forces have an attractive, as well as a repulsive component. Therefore it is possible to conclude that the electromagnetic forces are the source of all intermolecular interactions, including all adhesion forces.

The intermolecular forces described in the previous paragraph can be organized into three distinct categories: electrostatic forces, polarization forces, and quantum mechanical forces. The electrostatic forces involve all interactions between charges, dipoles, quadrupoles, etc. The electric field of such charges and permanent dipoles are also capable of inducing a dipole moment in nearby atoms or molecules. The forces between the induced dipole and the charge or dipole that induced it, are called polarization forces. These two categories of intermolecular forces lead to physical bonding. The last category, which consists of quantum mechanical forces, are responsible for chemical or covalent bonding. These three categories together comprise a wide variety of intermolecular interactions, as can be seen in figure 4.1.

### 4.1.1 Electrostatic Interactions

The first electrostatic interaction that will be discussed, is the well known Coulomb interaction between two charged atoms or molecules. This type of interaction has a very long range, as is illustrated by the expression for the Coulomb energy of two charges $q_1$ and $q_2$:

$$W = \frac{q_1 q_2}{4\pi\epsilon_0 r}, \tag{4.1}$$

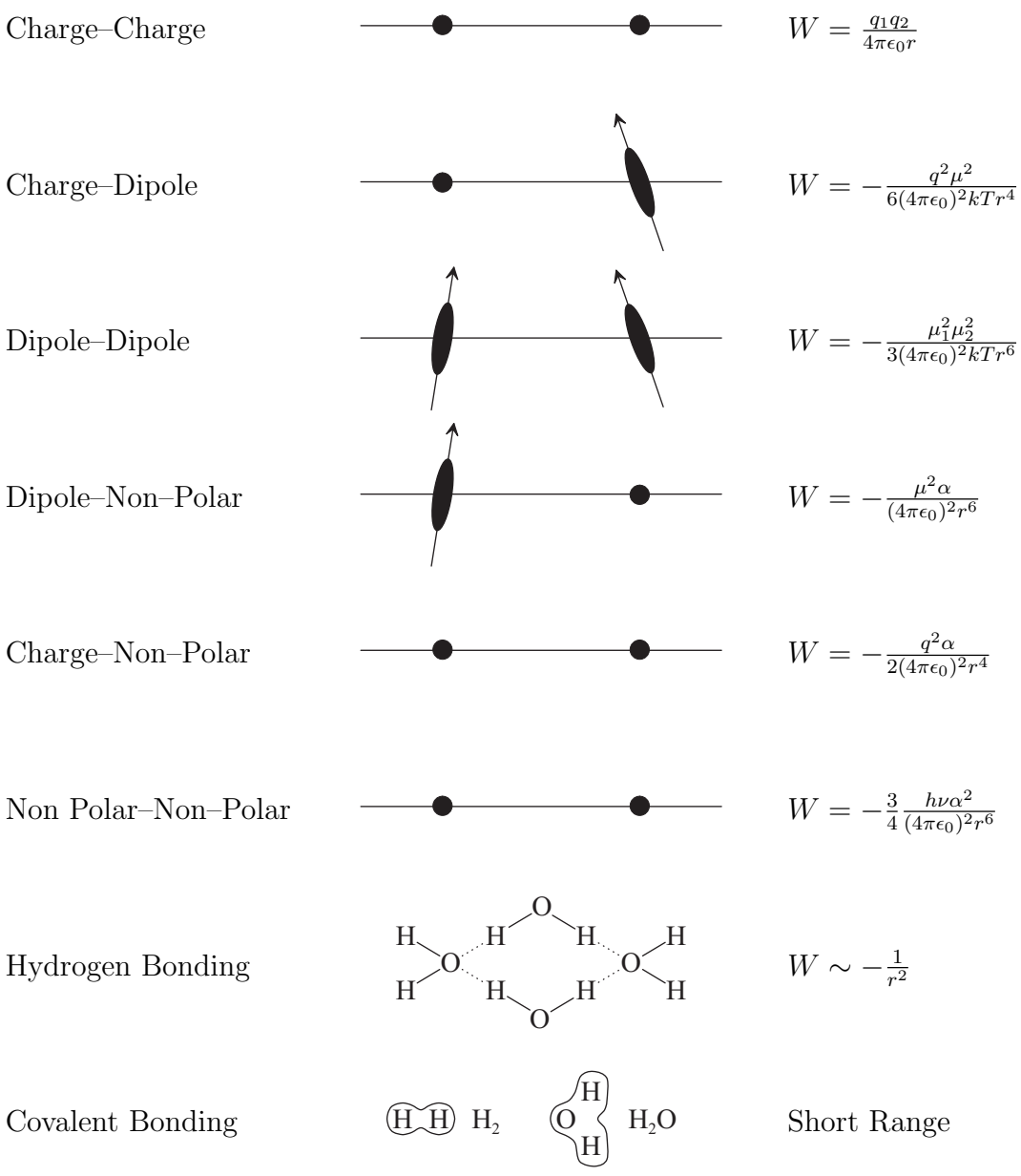


Figure 4.1: Overview of intermolecular interactions and their interaction energies. (Source: Intermolecular & Surface Forces [18], J. Israelachvili)

where $\epsilon_0$ is the permittivity of free space, and $r$ the distance between the two charges. An important example of this intermolecular force is the ionic bond between two oppositely charged ions.

But in most cases the Coulomb energy reduces to zero, because the majority of molecules is electrically neutral. In this case, it is still possible that some atoms, or groups within the molecule, have a higher affinity for electrons than the other groups or atoms. This property is called the electronegativity, and it causes a shift within the electron distribution of the molecule. The result is a so called polar molecule, which has a dipole moment due to its non–uniform charge distribution. The dipole moment of a polar molecule is a vector quantity, and is defined by the following integral:

$$\vec{\mu} = \int \rho(\vec{r}) \cdot \vec{r} \, \mathrm{d}V, \tag{4.2}$$

where $\rho(\vec{r})$ is the charge density at position $\vec{r}$. The interaction energy between two dipoles depends on their mutual orientation. To minimize their interaction energy, the dipoles have a tendency to align themselves parallel to each other. On the other hand, the alignment of the dipoles is randomized by the thermal energy $kT$. This results in the following expression for the interaction energy between two freely rotating dipoles:

$$W = -\frac{C_{\text{orient}}}{r^6} = -\frac{\mu_1^2 \mu_2^2}{3(4\pi\epsilon_0)^2 kT r^6}, \tag{4.3}$$

where $\mu_1$ and $\mu_2$ are the dipole moments of both molecules, $\epsilon_0$ the permittivity of free space, $kT$ the thermal energy, and $r$ the distance between the two dipoles. This type of interaction is often called the *Keesom* or *orientation* interaction. An example of a very strong Keesom interaction is *hydrogen bonding*. As can be seen in figure 4.1, the hydrogen bond in water is located between the negatively charged oxygen atom and the positively charged hydrogen atom (water is polar molecule). Because of the small size of the hydrogen atom, the distance between both atoms is much smaller than usual, which results in a very strong bond.

Another type of electrostatic interaction, is the interaction between a charge $q$ and a dipole $\mu$. In this case the dipole has the tendency to minimize its interaction energy by aligning itself towards or away from the charge, depending on the sign of the charge. This behavior is also randomized by the thermal energy $kT$, and the interaction energy is given by:

$$W = -\frac{q^2 \mu^2}{6(4\pi\epsilon_0)^2 kT r^4}, \tag{4.4}$$

where $\epsilon_0$ is the permittivity of free space, and $r$ the distance between the charge and the dipole.

### 4.1.2 Interactions Involving Polarization

At first, it might seem that there is no interaction between a dipole and a non–polar molecule. But the electric field produced by the dipole causes the electron distribution of the non–polar molecule to shift. This produces an induced dipole moment in the non–polar molecule, which can be calculated with:

$$\vec{\mu}_{\text{ind}} = \alpha \vec{E}, \tag{4.5}$$

where $\alpha$ is the polarizability, and $\vec{E}$ the electric field experienced by the non–polar molecule. The interaction between the permanent and the induced dipole is often called the *Debye* or *induction* interaction, and the corresponding interaction energy is given by:

$$W = -\frac{C_{\text{ind}}}{r^6} = -\frac{\mu^2 \alpha}{(4\pi\epsilon_0)^2 r^6}, \tag{4.6}$$

where $\mu$ is the dipole moment, $\epsilon_0$ the permittivity of free space, and $r$ the distance between the dipole and the non–polar molecule.

Another type of interaction that involves polarization, is the interaction between a charge and a non–polar molecule. In this case the charge is also able to induce a dipole in the non–polar molecule. The interaction energy between the charge and the induced dipole is given by:

$$W = -\frac{q^2 \alpha}{2(4\pi\epsilon_0)^2 r^4}, \tag{4.7}$$

where $q$ is the charge, $\alpha$ the polarizability, $\epsilon_0$ the permittivity of free space, and $r$ the distance between the charge and the induced dipole.

### 4.1.3 Quantum Mechanical Interactions

Until now it was possible to describe the various intermolecular interactions with the help of classical physics, but they fail to explain the intermolecular interaction between two non–polar molecules or atoms. The origin of this interaction can be understood by considering a non–polar atom, which consists of a positively charged nucleus and a negatively charged electron cloud. The electrons circle around the nucleus with a high frequency of approximately $10^{15}$ Hz, and at every instant the atom is therefore polar. When two of these oscillators are brought together, they will start to influence each other. In this case attractive orientations have a higher probability than repulsive ones, which leads to an attractive force. This type interaction is called the *London* or *dispersion* interaction, and the corresponding interaction energy can be calculated with quantum mechanical perturbation theory:

$$W = -\frac{C_{\text{disp}}}{r^6} = -\frac{3}{2}\frac{\alpha_1 \alpha_2}{(4\pi\epsilon_0)^2 r^6}\frac{h\nu_1\nu_2}{(\nu_1 + \nu_2)}, \tag{4.8}$$

where $\alpha_{1,2}$ is the electric polarizability, $\epsilon_0$ the permittivity of free space, $r$ the distance between the non polar molecules, $h$ Planck's constant, and $h\nu_{1,2}$ the ionization energy of the molecule or atom.

Covalent bonding is also quantum mechanical in nature, and it differs greatly from the previously discussed intermolecular interactions. These types of interactions were mostly based on electrostatics and polarization, whereas the covalent bond involves changes in the electron configuration of the two binding molecules. Covalent bonding is characterized by the sharing of pairs of electrons between atoms, as is illustrated in figure 4.1. The resulting bond is usually a very strong bond, with a typical energy that is well above the thermal energy $kT$.

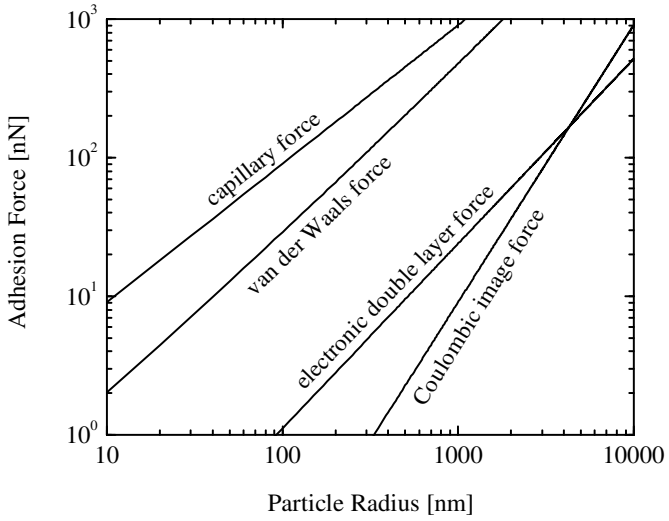


Figure 4.2: Comparison of the various types of macroscopic adhesion forces acting on a spherical particle on a flat surface. The capillary force was calculated for water, and the van der Waals force applies to polysterene latex (PSL) spheres on a silicon surface. Furthermore, the electronic double layer force was calculated for a contact potential of 0.5 V, and the Coulombic image force was calculated for a surface charge density of 1000 electrons/$\mu$m$^2$.

## 4.2 Adhesion Between Macroscopic Bodies

After a short overview of the most important intermolecular interactions, it is now time to take a look at various adhesion forces between macroscopic bodies. As will be shown in the following subsections, the *van der Waals* and the *capillary* force are the two most important forces to consider, when studying the adhesive properties of sub–micrometer particles on a flat surface. This is also illustrated by figure 4.2, which shows the magnitude of various types of adhesion forces as a function of the particle diameter.

### 4.2.1 van der Waals Forces

The first adhesion force that will be discussed is the *van der Waals* force. This force is a combination of the orientation, induction, and dispersion forces, which have the same $r^{-6}$ distance dependence. When all three interactions are summed, the following expression is found for the van der Waals energy between two single molecules:

$$W_{\mathrm{vdW}} = -\frac{C_{\mathrm{orient}} + C_{\mathrm{ind}} + C_{\mathrm{disp}}}{r^6} = -\frac{C}{r^6}, \tag{4.9}$$

where $r$ is the distance between both molecules. To calculate the van der Waals energy between two macroscopic bodies, it is convenient to assume that the van der Waals interaction energies are additive. This can be illustrated by calculating the van der Waals energy of a single molecule at a distance $D$ away from a flat surface. The molecule interacts with the other molecules in the surface, and the sum of all the individual interactions gives the total van der Waals energy. If the molecular density of the surface is equal to $\rho$, it is possible to express the total van der Waals energy in a single integral. Figure 4.3a

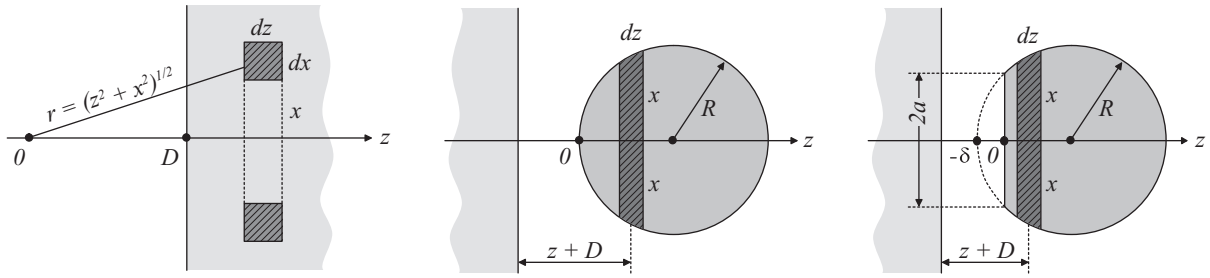


(a) (b) (c)

Figure 4.3: Integration paths to calculate the interaction energy between (a) a molecule and an infinitely large surface. (b) a sphere and an infinitely large surface. (c) a deformed sphere and an infinitely large surface.

shows that the surface can be divided into a collection of infinitesimal thick rings. Each ring contains $2\pi x\rho\ \mathrm{d}x\ \mathrm{d}z$ molecules, and the interaction energy can be calculated with the following integral:

$$\begin{aligned} W &= \int_D^\infty \mathrm{d}z \int_0^\infty 2\pi x\rho \left(-\frac{C}{r^6}\right)\ \mathrm{d}x \\ &= -2\pi C\rho \int_D^\infty \mathrm{d}z \int_0^\infty \frac{x}{(x^2+z^2)^3}\ \mathrm{d}x \\ &= -2\pi C\rho \int_D^\infty \frac{1}{4z^4}\ \mathrm{d}z \\ &= -\frac{\pi C\rho}{6D^3}. \end{aligned} \tag{4.10}$$

This result can now be used to calculate the van der Waals energy between a surface and a spherical particle. In this case the sperical particle is divided into a collection of slices, as can be seen in figure 4.3b. The number of molecules contained in an infintesimal thin slice is equal to $z(2R-z)\pi\rho_1\ \mathrm{d}z$. This gives the following integral:

$$\begin{aligned} W &= \int_0^{2R} z(2R-z)\pi\rho_1 \left(-\frac{\pi\rho_2 C}{6(z+D)^3}\right)\ \mathrm{d}z \\ &= -\frac{\pi^2\rho_1\rho_2 C}{6} \int_0^{2R} \frac{z(2R-z)}{(z+D)^3}\ \mathrm{d}z, \end{aligned} \tag{4.11}$$

where $\rho_1$ and $\rho_2$ are the molecular density of the surface and the sphere respectively. The distance $D$ is typically in the order of 4 Å, which is much smaller than the radius $R$ of the particle itself. Therefore, only small values of $z$ will contribute to the integral. In this case the integral can be simplified as follows:

$$\begin{aligned} W &= -\frac{\pi^2\rho_1\rho_2 C}{6} \int_0^\infty \frac{2Rz}{(z+D)^3}\ \mathrm{d}z \\ &= -\frac{\pi^2\rho_1\rho_2 CR}{6D}. \end{aligned} \tag{4.12}$$

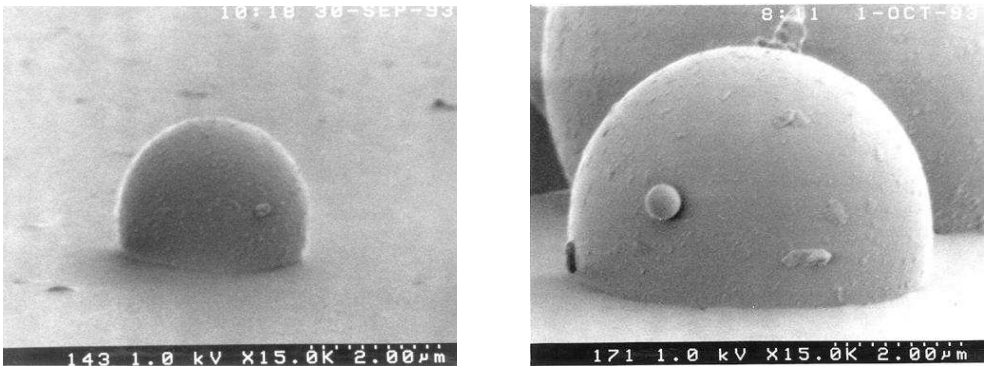


Figure 4.4: Scanning Electron Microscope (SEM) pictures of adhesion induced deformation of small spherical particles. (Source: Lecture Notes Particle Deposition, Transport & Removal, Clarkson University [19].)

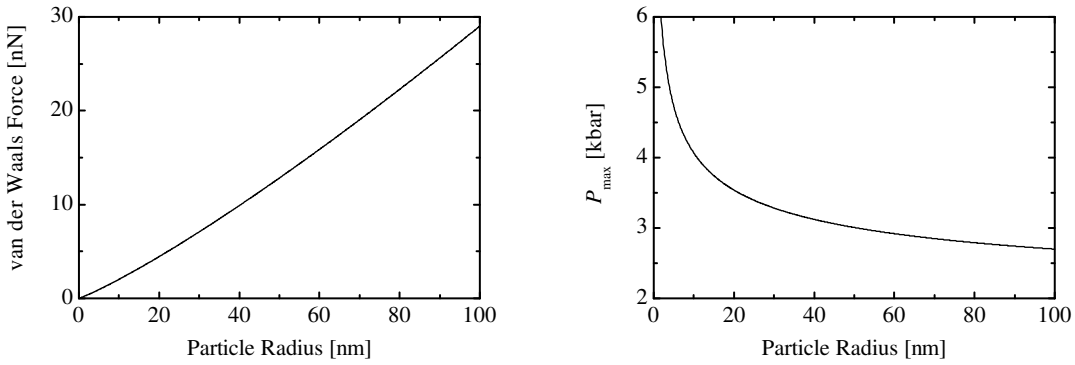


Figure 4.5: Two graphs showing the van der Waals force and the resulting pressure in the contact area between the particle and the surface as a function of the particle radius.

The van der Waals force can be calculated from equation (4.12) in a relatively straightforward manner:

$$F_{\mathrm{vdW}} = -\frac{\partial W}{\partial D} = \frac{AR}{6D^2}, \tag{4.13}$$

where $A = \pi^2 \rho_1 \rho_2 C$ is the Hamaker constant. For most materials the Hamaker constant does not vary much, and has a typical value of ($10^{-19}$–$10^{-20}$) J.

Depending on the mechanical properties of the materials involved, the van der Waals force can be strong enough to deform the particle. This creates a circular contact area with radius $a$ at the interface between the particle and the surface. The interaction energy can be calculated by adjusting equation (4.12) to the integration path shown in figure 4.3c:

$$\begin{aligned} W &= -\frac{\pi^2 \rho_1 \rho_2 C}{6} \int_0^\infty \frac{2R(z+\delta)}{(z+D)^3}\,\mathrm{d}z \\ &= -\frac{\pi^2 \rho_1 \rho_2 C}{6}\left(\frac{1}{D} + \frac{\delta}{D^2}\right). \end{aligned} \tag{4.14}$$

For small values of $\delta$ it is possible to write down the following simple geometric relationship

between the contact radius $a$, the particle radius $R$, and the deformation length $\delta$:

$$a^2 = R^2 - (R-\delta)^2 = 2\delta R - \delta^2 \approx 2\delta R \quad \Rightarrow \quad \delta = \frac{a^2}{2R}. \tag{4.15}$$

Substituting this into equation (4.14) and taking the derivative gives the van der Waals force for a deformed sphere on a flat surface:

$$F_{\mathrm{vdW}} = -\frac{\partial W}{\partial D} = \frac{AR}{6D^2}\left(1 + \frac{a^2}{RD}\right), \tag{4.16}$$

where the second term between the parentheses accounts for the deformation of the particle. The relationship between the contact radius and the particle radius is given by:

$$a^3 = \left(\frac{AR^2}{6KD^2}\right), \qquad K = \frac{4}{3}\left(\frac{1-\nu_1^2}{E_1} + \frac{1-\nu_2^2}{E_2}\right)^{-1}, \tag{4.17}$$

where $\nu_{1,2}$ and $E_{1,2}$ are the Poisson coefficients and Young's modulus of the particle (1) and the surface (2). This relationship was first derived by Derjaguin[20], and it makes it possible to plot the van der Waals force as a function of the particle radius by combining equation (4.16) and (4.17). Even though the van der Waals force decreases for smaller particles, the pressure in the contact area can reach very high values. According to Hertz [21], the pressure distribution has a parabolic shape, and it can be calculated with the following expression:

$$P(r) = P_{\max}\left(1 - \frac{r^2}{a^2}\right), \qquad P_{\max} = \frac{3}{2}\frac{F}{\pi a^2}, \tag{4.18}$$

where $F$ is the force on the particle. To put this into perspective, two plots of the van der Waals force and the contact pressure are shown in figure 4.5. These plots show that the contact pressure increases to very high values for small particles, even though the van der Waals force decreases. Smaller particles are therefore more difficult to remove with LSC, because they require a larger pressure jump across the shockwave.

### 4.2.2 Capillary Forces

Another important macroscopic adhesion force is the *capillary force*. This force is the result of capillary condensation of moisture in the small cracks and crevices that surround the contact area, as can be seen in figure 4.6. Capillary condensation is a phenomenon that allows vapor to condensate, even though the vapor pressure is well below the equilibrium vapor pressure of the liquid. This is possible because the surface of the liquid in figure 4.6 is curved, which causes the value of the equilibrium vapor pressure to change. The change in equilibrium vapor pressure of a curved liquid surface can be calculated with the *Kelvin equation*, which gives the ratio $p_{\mathrm{c}}/p_{\mathrm{p}}$ between the equilibrium vapor pressure of a curved and a planar surface:

$$\ln\left(\frac{p_{\mathrm{c}}}{p_{\mathrm{p}}}\right) = \frac{\gamma V_{\mathrm{m}}}{RT}\left(\frac{1}{R_1} + \frac{1}{R_2}\right), \tag{4.19}$$

where $R_1$ and $R_2$ are the two principal radii of curvature, $\gamma$ the surface tension of the liquid, $V_{\mathrm{m}}$ the molar volume of the liquid, $R$ the gas constant, and $T$ the temperature.

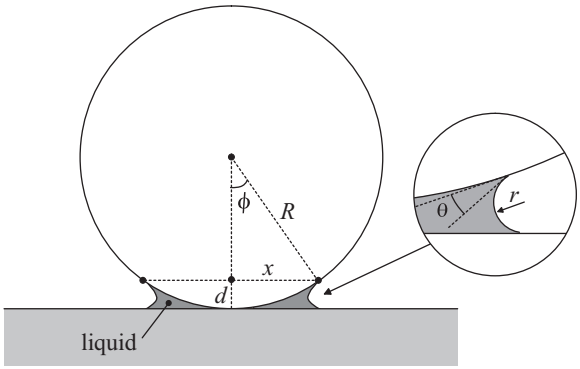


Figure 4.6: Capillary condensation of moisture in the cracks and crevices around the contact area.

The radius of curvature is defined as positive when the interface is curved towards the liquid, and negative when the interface is curved in the opposite direction. Applying the Kelvin equation to the situation sketched in figure 4.6 yields the following expression:

$$\ln\left(\frac{p_\mathrm{c}}{p_\mathrm{p}}\right) = \frac{\gamma V_\mathrm{m}}{RT}\left(\frac{1}{x} - \frac{1}{r}\right). \tag{4.20}$$

In general it is safe to assume that $x >> r$, and the previous equation can be rewritten into the following form:

$$\ln\left(\frac{p_\mathrm{c}}{p_\mathrm{p}}\right) = -\frac{\gamma V_\mathrm{m}}{RT}\left(\frac{1}{r}\right), \tag{4.21}$$

which shows that the equilibrium vapor pressure of the negatively curved liquid is smaller than that of a planar surface. This explains why vapor is able to condensate in small cracks and crevices at vapor pressures well below the equilibrium vapor pressure $p_\mathrm{p}$.

The curvature of the fluid is the result of a pressure difference inside and outside the liquid. This pressure difference is called the *Laplace pressure*, and it is calculated in the following way:

$$\Delta p = \gamma\left(\frac{1}{R_1} + \frac{1}{R_2}\right), \tag{4.22}$$

where $R_1$ and $R_2$ are the two principal radii of curvature again, and $\gamma$ the surface tension of the liquid. Applying this to the curved liquid in figure 4.6 yields the following expression for the Laplace pressure:

$$\Delta p = \gamma\left(\frac{1}{x} - \frac{1}{r}\right) \approx -\gamma\left(\frac{1}{r}\right). \tag{4.23}$$

This shows that the pressure inside the liquid is smaller than the pressure of the surrounding air. The pressure difference acts on an area[1] $\pi x^2 \approx 2\pi Rd$ between the two surfaces,

[1] Pythagoras: $R^2 = x^2 + (R-d)^2 \quad \Rightarrow \quad x^2 = 2Rd - d^2 \approx 2Rd$.

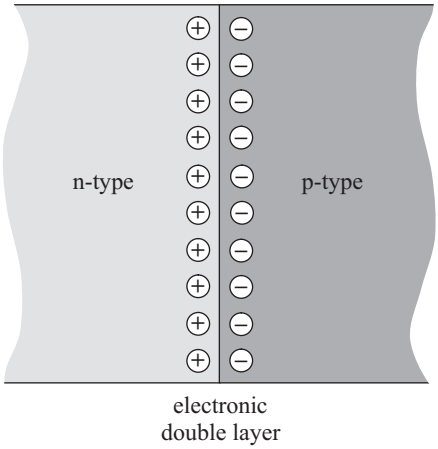


Figure 4.7: Schematic sketch of the electronic double layer that forms at the interface of a p–n junction between two semiconductors.

and the resulting adhesion force $2\pi\gamma Rd/r$ is called the capillary force. For small values of $\phi$ the approximation $d \approx 2r\cos\theta$ can be used to find the following expression for the capillary force between a sphere and a flat surface:

$$F_{\text{cap}} = 4\pi\gamma R\cos\theta, \tag{4.24}$$

where $\theta$ is the contact angle between the liquid and the surface of the sphere, as indicated in figure 4.6.

### 4.2.3 Electronic Double Layer Forces

The third macroscopic adhesion force that will be discussed is the electronic double layer force. This force arises when two solids charge each other electrostatically when they come into contact with one another. This phenomenon is often called the *triboelectric effect*, because in some cases it can be enhanced by rubbing the two materials together (*tribos* is greek for rubbing). The result of the electrostatic charging is a so called electronic double layer at the interface between the two solids. The mechanism responsible for the charge transfer between the two solids is diverse, and it depends on a wide variety of properties such as the material, surface roughness and temperature.

A good example to demonstrate the formation of an electronic double layer is a p–n junction between two semiconductor materials. Upon contact, the electrons and holes will migrate from one material to the other, due to the difference in concentration. This process will continue until the potential difference, that develops between the two materials due to the charge separation, has grown large enough to stop any further migration of charge carriers. The result is an electronic double layer at the interface between the two solids, as can be seen in figure 4.7. The potential difference between the two materials is called the contact potential, and its maximum value is about 0.5 V [22]. The resulting electronic double layer force at the contact area between a spherical particle and a flat surface can be calculated with [22]:

$$F_{\text{edl}} = \frac{\pi a^2\epsilon_0 U^2}{2D^2}, \tag{4.25}$$

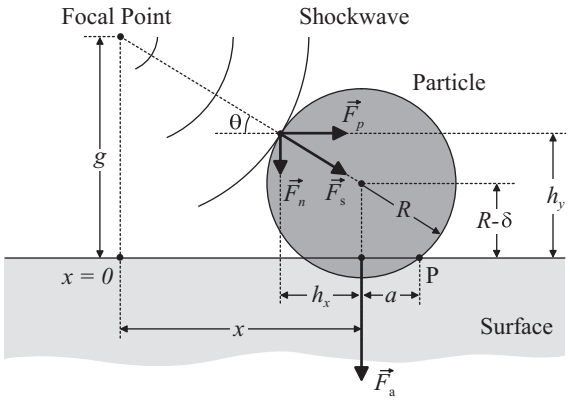


Figure 4.8: Geometry used in the particle removal model.

where $a$ is the contact radius, $\epsilon_0$ the permittivity of free space, $U$ the contact potential, and $D$ the separation between the particle and the surface at the contact area (4 Å).

### 4.2.4 Coulombic Image Forces

The last macroscopic adhesion force that will be discussed, is the Coulomb force that exists between a charged sphere and the surface charge that it induces in an electrically neutral flat surface. From electrostatic theory it is known, that the electric field produced by the electrostatic induction and the charged sphere is identical to the electric field produced by two oppositely charged point charges. The force between the surface and the sphere is therefore equal to the force between two oppositely charged point charges separated by a distance $2r$. This force is often called the Coulombic image force, and it can be calculated with:

$$F_{\text{cif}} = \frac{q^2}{16\pi\epsilon_0 r^2}, \tag{4.26}$$

where $q$ is the charge of the sphere, $\epsilon_0$ the permittivity of free space, and $r$ the radius of the sphere.

## 4.3 Particle Removal Model

Now that the most important adhesion forces have been identified in the previous section, it is time to create a particle removal model that is able to predict the cleaning performance of the LSC method. The main goal of this model will be to predict the diameter of the smallest particle that can be removed with LSC.

### 4.3.1 Definitions and Implementation

The particle removal model presented in this section is based on the geometry sketched in figure 4.8. In this figure the LIB is created at a distance $g$ above the surface, which is commonly referred to as the *gap distance*. In the model, the shockwave produced by the LIB expands spherically, and travels over a distance $r$ before it reaches the center of the

particle. The particle itself is assumed to be spherical, which simplifies the calculations significantly. When the shockwave passes the particle, it experiences a pressure jump $\Delta p$, which can be calculated with equation (2.34). The resulting shock force $F_\mathrm{s}$ on the particle is composed of a normal component $F_\mathrm{n}$ and a parallel component $F_\mathrm{p}$. The external load applied to the particle by the normal component $F_\mathrm{n}$ causes the contact radius to change. In this case equation (4.17) is no longer sufficient, and the contact radius must be calculated with the help of the Johnson–Kendall–Roberts (JKR) theory [23]:

$$a^3 = \frac{R}{K}\left(P + 3\pi W_\mathrm{a} R + \sqrt{6\pi W_\mathrm{a} R P + (3\pi W_\mathrm{a} R)^2}\right) \tag{4.27}$$

where $W_\mathrm{a}$ is the surface energy, $P$ the external load, and $K$ is defined by equation (4.17). The surface energy $W_\mathrm{a}$ refers to the van der Waals interaction energy between the two flat surfaces at the contact area:

$$W_\mathrm{a} = \frac{A}{12\pi D^2}, \tag{4.28}$$

where $A$ is the Hamaker constant, and $D$ the distance between the particle and the surface (typically 4 Å). In addition to the contact radius, the deformation length also changes as a result of the external load:

$$\delta = \frac{a^2}{R}\left(1 - \frac{2}{3}\left(\frac{a_0}{a}\right)^{3/2}\right), \tag{4.29}$$

where $a_0$ is the JKR contact radius when there is zero external load on the sphere:

$$a_0 = \left(\frac{6\pi W_\mathrm{a} R^2}{K}\right)^{1/3}. \tag{4.30}$$

It should also be remembered, that under certain circumstances the particle is also subjected to capillary forces, which increases the total adhesion force and causes additional deformation of the particle. All the forces that have been discussed until now, excert two different moments on the particle:

$$M_\mathrm{c} = F_\mathrm{p} \cdot h_y, \tag{4.31}$$

$$M_\mathrm{a} = F_\mathrm{n} \cdot (h_x + a) + (F_\mathrm{vdW} + F_\mathrm{cap}) \cdot a, \tag{4.32}$$

where $M_\mathrm{c}$ is the cleaning moment, $M_\mathrm{a}$ the adhesion moment, $F_\mathrm{vdW}$ the van der Waals force, and $F_\mathrm{cap}$ the capillary force. When the cleaning moment $M_\mathrm{c}$ is larger than the adhesion moment $M_\mathrm{a}$, a rolling motion of the particle is initiated. The cleaning condition is thus:

$$\frac{M_\mathrm{c}}{M_\mathrm{a}} > 1. \tag{4.33}$$

Finally, it should also be noted that the thickness of the shock front is in the order of the mean free path length (see equation (2.15)), which is 68 nm for air at atmospheric pressure. This means that in some cases the size of the particle is comparable to the thickness of the shock front, which can be a problem since the model assumes a continuous medium. Despite this, the model was still able to make an accurate prediction of the diameter of the smallest removable particle, as can be seen in the next subsection.

As mentioned before, the main goal of this model is to predict the diameter of the smallest particle that can be removed for a given gap distance $g$ and shockwave energy $W$. The algorithm that has been used is outlined in two separate flow charts, which can be found in figure 4.9 and 4.10. The first flow chart shows an overview of the main program, while the second flow chart gives a detailed view of the algorithm that was used to calculate $M_c/M_a$. In short, the program iterates through a range of gap distances and shockwave energies, and checks whether or not cleaning condition (4.33) is satisfied. The complete program was implemented in MATLAB©, and the source code can be found in appendix A.

As can be seen in figure 4.10, the calculation of all the variables in this model is not straightforward, since some variables are interdependent. This can be clearly seen in the calculation of the van der Waals force on the particle. First, both the contact radius $a$ and the deformation length $\delta$ are estimated. This defines the distance between the particle and the LIB, which makes it possible to calculate the shock force on the particle. But the particle is deformed by the shock force, and this means that both $a$ and $\delta$ will have to be recalculated. The new values of $a$ and $\delta$ are then compared to the old values, to see if the original estimate was a good one. If this is not the case, the newly calculated values will be used as new estimates, and the whole procedure repeats itself. This strategy will result in an iterative procedure, in which the values of these variables can converge to their final values.

### 4.3.2 Simulation Results

The particle removal model presented in the previous subsection was applied to the case of polystyrene latex spheres on a silicon surface. Figure 4.11 shows the results of these simulations, in the form of a collection of contour plots. These contour plots show that the gap distance has a much stronger influence on the cleaning performance of LSC than the shockwave energy, as was expected on the basis of equation (2.34). Furthermore, the first contour plot shows that for a typical set of parameters ($W = 115$ mJ, $g = 0.5$ mm) the smallest removable particle has a diameter somewhere between 30 and 60 nm. This prediction was later confirmed by the cleaning experiments presented in the next chapter. Unfortunately, this result is not good enough for the cleaning of EUV reticles, because the diameter of the smallest removable particle still exceeds 30 nm. This changes however, when the capillary forces are eliminated from the model, as can be seen in the second contour plot of figure 4.11. In this case it is predicted, that the diameter of the smallest removable particle lies well below 30 nm.

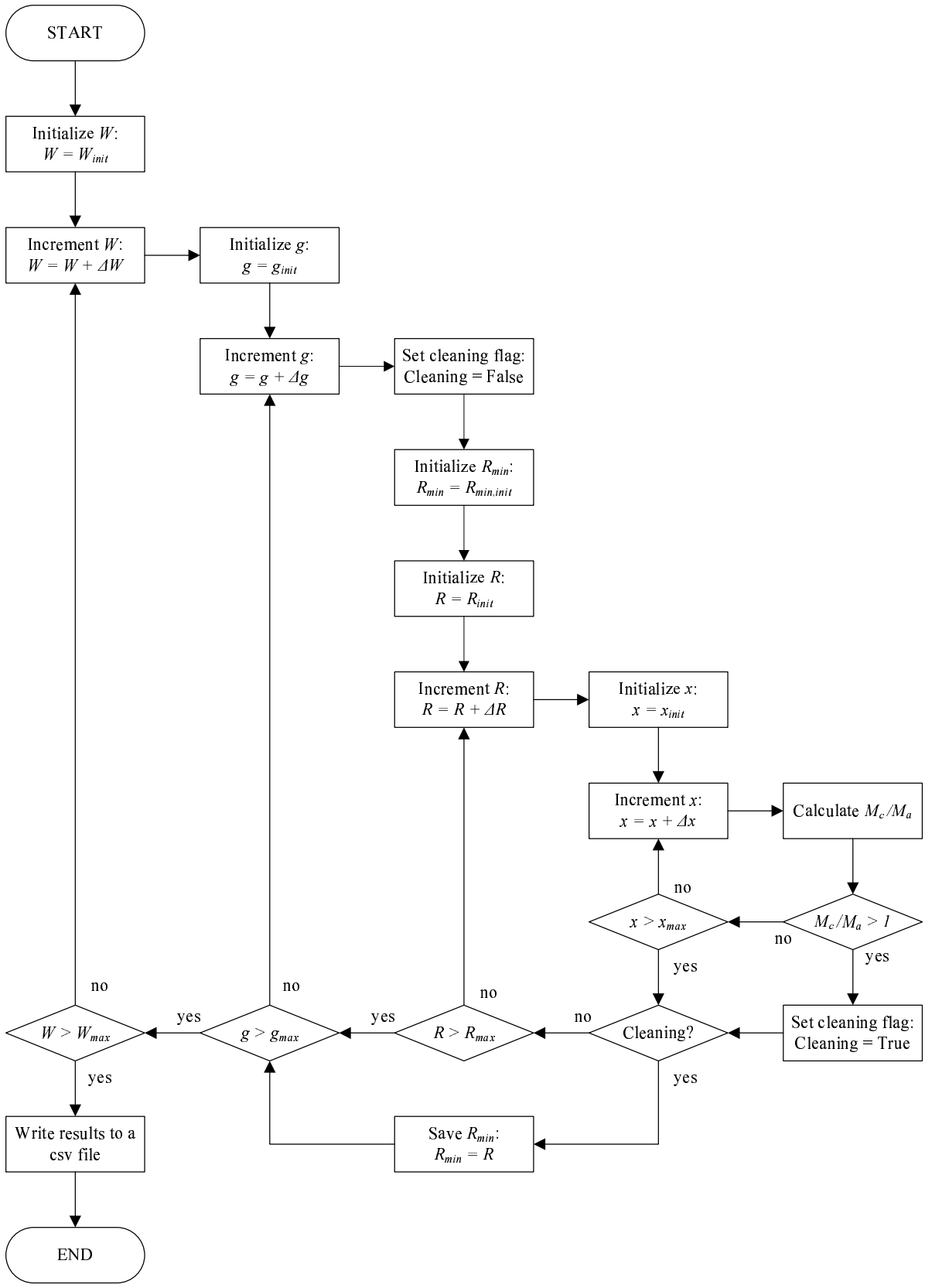


Figure 4.9: Flow chart of the MATLAB© script that was used to calculate the diameter of the smallest removable particle for a range of gap distances and shockwave energies. The separate flow chart of the calculation of $M_c/M_a$ can be found in figure 4.10

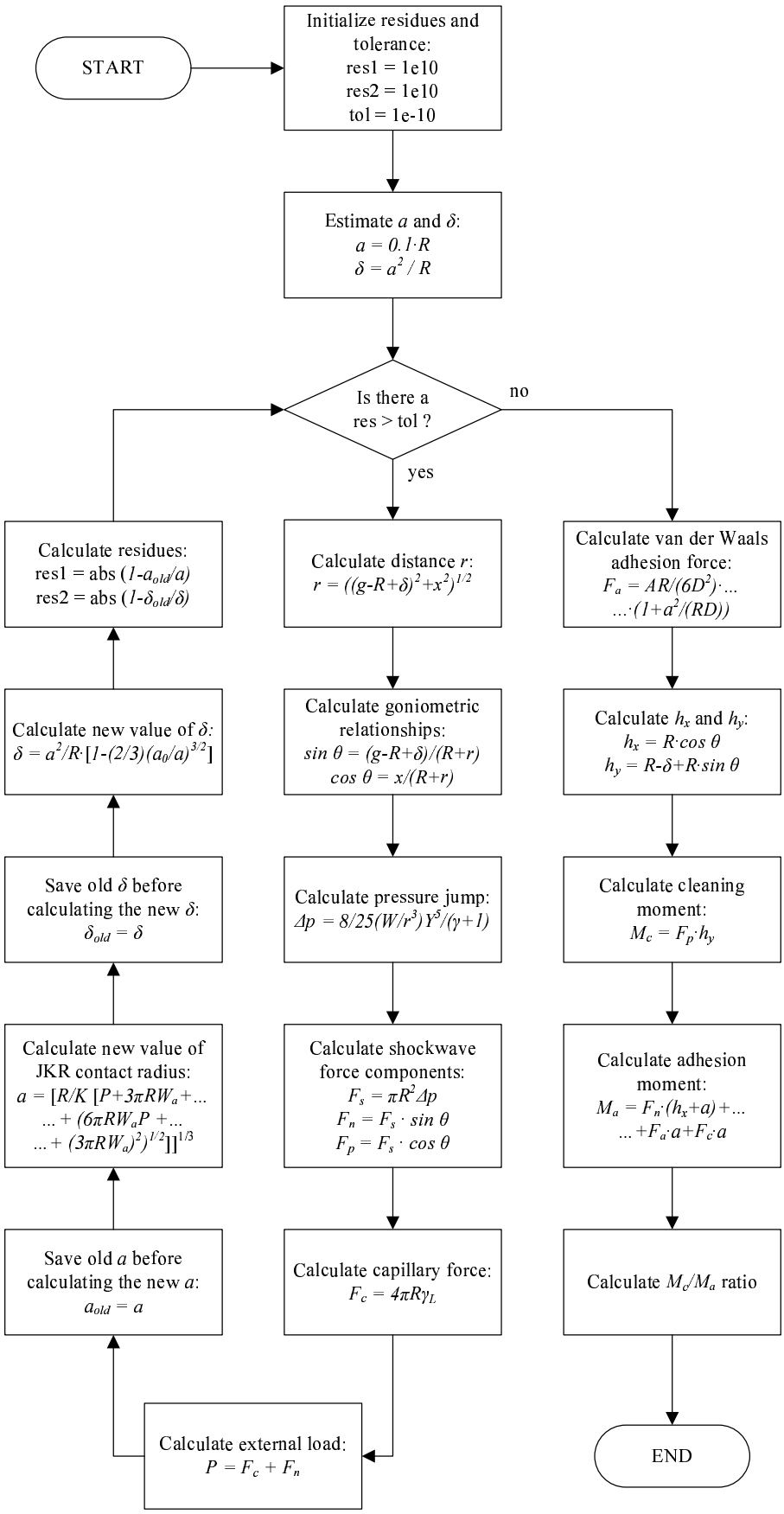


Figure 4.10: Flow chart of the MATLAB© script that was used to calculate the ratio between the cleaning moment and the adhesion moment.

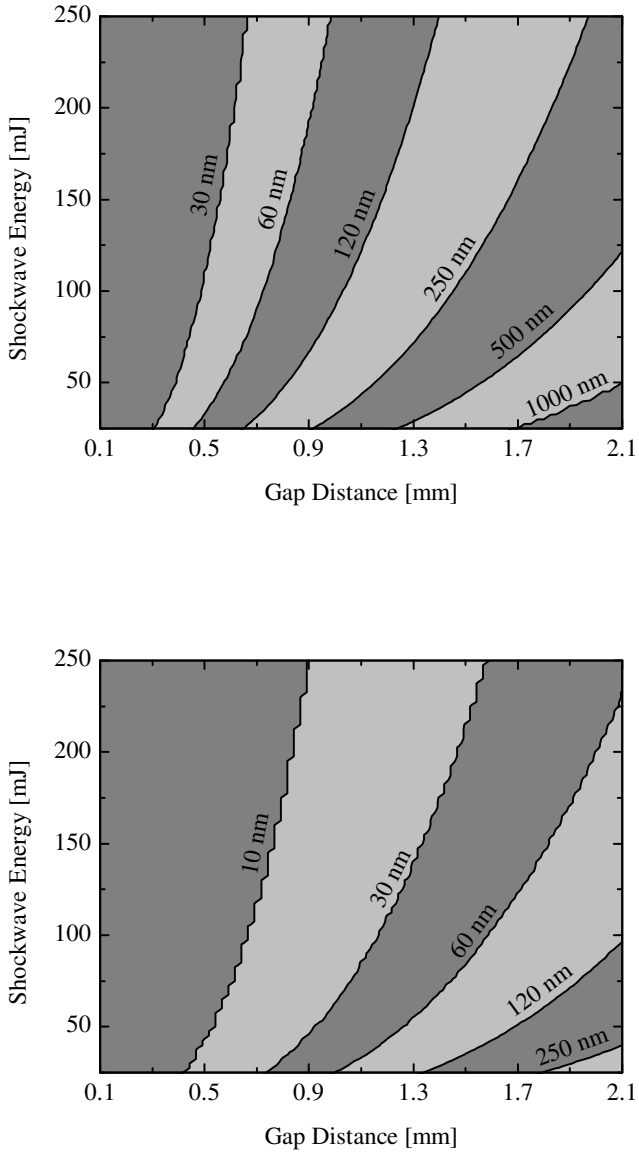


Figure 4.11: Contour plots showing the diameter of the smallest polystyrene latex particle that can be removed from a silicon surface for a range of shockwave energies $W$ and gap distances $g$. The first plot also takes the capillary forces into account, while the second plot at the bottom only considers the van der Waals force.

# 5 Cleaning Experiments

Since this thesis is about particle removal, it would not be complete without a series of cleaning experiments. These cleaning experiments involved the removal of polysterene latex (PSL) and $SiO_2$ spheres from flat 1 inch unpatterned silicon wafers. Special attention is also given to the deposition and detection of sub–micrometer particles, since these two processes are important prerequisites for succesfull cleaning experiments. The results of these experiments showed that it was possible to remove particles as small as 50 nm with LSC. It was however not possible to remove particles as small as 30 nm, which is in agreement with the theoretical particle removal model presented in the previous chapter.

## 5.1 Laser Shockwave Cleaning Setup

Before looking at the particle deposition and detection methods, this section will shortly discuss the experimental setup that was used for the cleaning experiments. Besides an overview, this section will also include a discussion about some important limitations of the setup, that might be of importance to the future application of LSC.

### 5.1.1 General Overview

The setup that was used for the cleaning experiments presented in this chapter is relatively simple, as can be seen in figure 5.1. The setup consists of a 1064 nm Q–switched Nd:YAG laser, a plano–convex lens with a focal lengh of 75 mm, and a micrometer table to accurately control the position and gap distance. The Nd:YAG laser had a $1/e^2$ beam diameter of 5 mm and a FWHM pulse length of 6 ns. This particular laser is the same laser that was already used to create the LIB for the imaging experiments in chapter 3. The complete setup was mounted on an optical table, which was located in an ISO class 6 cleanroom. Furthermore, the LIB was created in normal air at atmospheric pressure and room temperature.

Figure 5.1: Picture of the LSC setup that was used for the cleaning experiments. The setup consists of a Q–switched Nd:YAG laser, a single plano–convex $CaF_2$ lens, and a micrometer controlled xyz–stage.

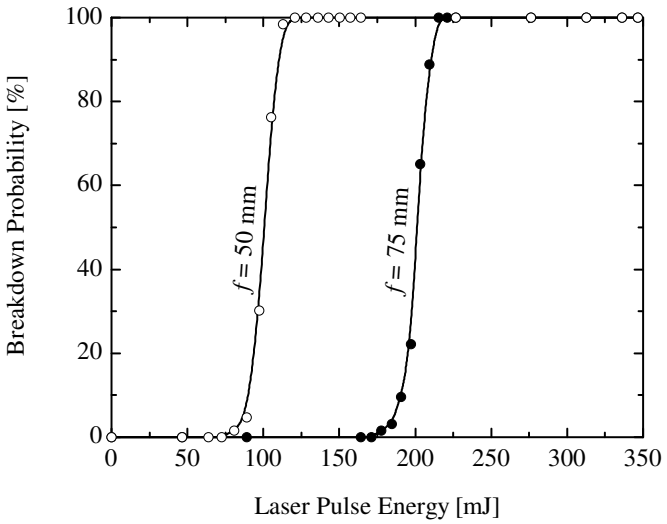


Figure 5.2: Measured breakdown probability for two lenses with different focal lengths. The breakdown probability is defined as the ratio between the number of successful breakdowns and the number of laser pulses.

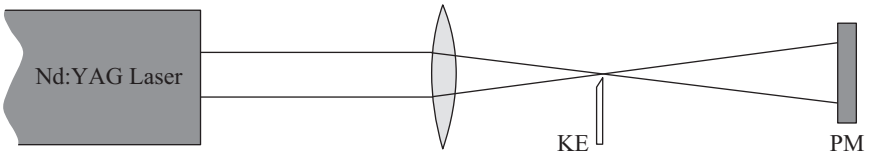


Figure 5.3: Schematic sketch of the setup that was used to measure the diameter of the focal spot. The knife edge (KE) is mounted on a micrometer controlled stage, and is able to slide into the focal point of the lens. The power meter (PM) is used to measure the amount of light that is able to pass the knife edge.

### 5.1.2 Limitations

The LSC setup presented in the previous subsection is limited in several ways. One of these limitations is the inability of the setup to produce LIB at low laser pulse energies. As was shown in chapter 2, there is a minimum threshold intensity that has to be achieved before LIB can be initiated. The existence of such a threshold intensity can be clearly seen in figure 5.2, which shows the breakdown probability as a function of the laser pulse energy. The figure shows that the breakdown probability changes very abruptly, when the laser pulse energy falls below a certain threshold value. As can be seen in figure 5.2, this threshold value is higher for lenses with longer focal lengths, than for lenses with shorter focal lengths. This can be explained by the fact that lenses with a shorter focal length are able to produce a smaller focal spot.

This was confirmed by an experiment, in which a knife edge was used to measure the focal spot diameter of both lenses. Figure 5.3 shows a schematic sketch of the setup that was used. The knife edge is mounted on a micrometer controlled stage, and is able to

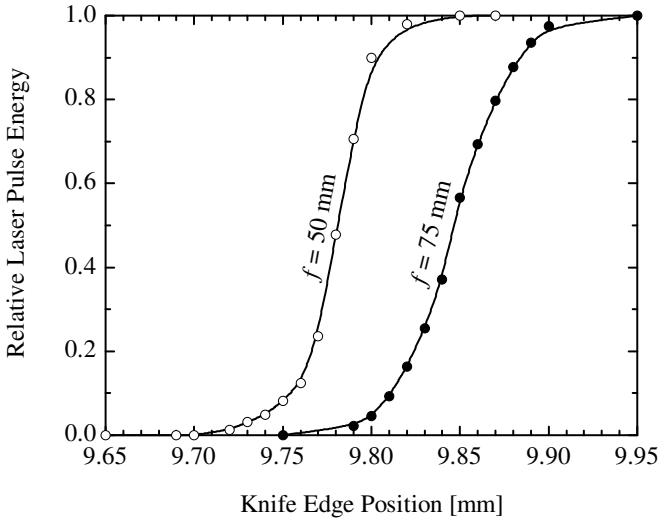


Figure 5.4: Results of the knife edge experiment, which shows that the lens with the 50 mm focal length produces a smaller focal spot than the lens with the 75 mm focal length.

slide into the focal point of the lens. The laser power meter behind the knife edge is used to measure the amount of laser light as a function of the position of the knife edge. The results of this experiment are plotted in figure 5.4, and show that the intensity distribution in the focal point is gaussian for both lenses. From this figure the $1/e^2$ diameter of both focal spots were determined, which were found to be 44 and 62 $\mu$m for a focal length of 50 and 75 mm respectively. These numbers result in a threshold intensity of $3.5{\cdot}10^{11}$ W/cm$^2$, which is close to the typical threshold intensity predicted by equation (2.11).

Another important limitation of the LSC setup is the low repetition rate at which the LIB can be created. Experiments have shown that in normal air at atmospheric pressure and room temperature, the maximum repetition frequency is approximately 4 Hz for a lens with a focal length of 75 mm. When the repetition frequency approaches this maximum value, the breakdown probability drops to zero very rapidly. This limitation in repetition frequency might be caused by the turbulence left by the previous LIB, which prevents proper focusing of the next laser pulse. Unfortunately, the maximum repetition frequency of the setup is still far too low to clean a complete reticle of $(15 \times 15)$ cm$^2$ within a reasonable amount of time (less than 10 minutes). This is a very severe limitation of the current setup, which has to be solved to make LSC a practical cleaning method for EUV reticles.

## 5.2 Particle Deposition Methods

As mentioned at the beginning of this chapter, particle deposition is a crucial part of the cleaning experiments. The particles have to be deposited in such a way, that the particles do not form clusters but are nicely monodispersed. Furthermore, special care has to be taken to ensure, that only one size of particles is deposited on the wafer, because some detection methods are only able to detect the presence of a particle, and not the size. This makes the deposition of particles a non–trivial task. The deposition methods that were

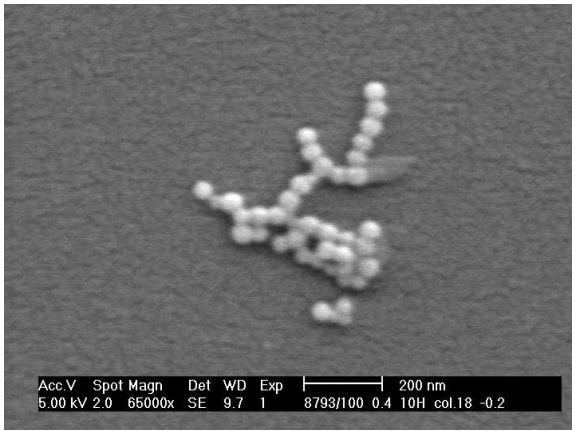


Figure 5.5: Scanning Electron Microscope (SEM) image of 50 nm particles clustered together by the van der Waals force.

used for the cleaning experiments presented in this chapter are *spin coating* and *aerosol spraying*. Both methods will be explained in the following two subsections.

### 5.2.1 Spin Coating

The first method of particle deposition that will be discussed is *spin coating*. This deposition method consists of several steps, which have to be followed in a specific order to obtain reproducable and reliable results. First, all the particle stock solutions (manufacturer: Duke Scientific) were placed in a megasonic bath for 15 minutes, to break up any clusters of particles in the solution. This is necessary, because small sub–micrometer particles tend to coagulate under the influence of the van der Waals force (see figure 5.5). After the stock solution was sonicated, it was diluted with either water or isopropanol alcohol, before it was sonicated again. This process was repeated until the particle concentration of the solution had reached the desired value. A small amount of solution was then dropped onto the center of a wafer, which was rotating in the spin coater at approximately 6100 rpm. Under the influence of the centrifugal force, the particle solution spread out very rapidly over the surface of the wafer, resulting in a sample with nicely monodispered particles. To improve its wetting properties, the wafer was put in an UV ozone reactor for three minutes before it was spin coated.

As the previous paragraph shows, spin coating can be a slow and tedious process, especially when the recipe involves many dilution steps. Recipes for each type of particle (material and size) have to be found by trial and error. On the other hand, this method produced excellent samples with monodispersed particles down to 50 nm. Depositing smaller particles with this method is however not advisable because of particle clustering.

### 5.2.2 Aerosol Spraying

Another method of particle deposition is *aerosol spraying*, which was done with the particle deposition tool shown in figure 5.6. This method of particle deposition is much simpler and faster than spin coating, once the equipment has been set up. The main component of the particle deposition tool is the *atomizer*, which transforms the particle solution into an aerosol. This aerosol is then redirected through a series of tubes and expansion cham-

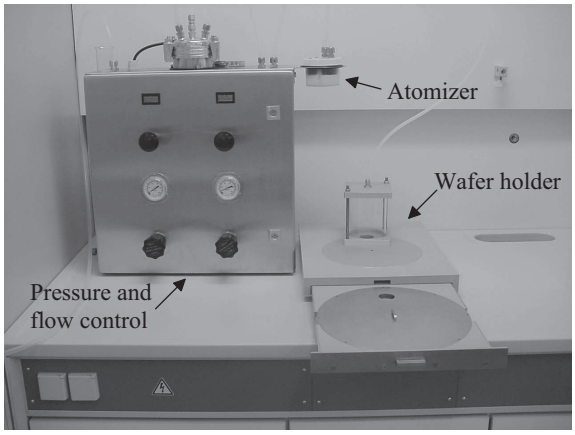


Figure 5.6: Picture of the particle deposition tool. The main component of the deposition tool is the atomizer, which transforms the particle solution into an aerosol.

bers, before it is brought into contact with the wafer. This method of deposition is much more suitable for the deposition of very small particles below 100 nm, because it is less sensitive to clustering.

## 5.3 Particle Detection Methods

Besides cleaning, inspection also plays an important role in the experiments presented in this chapter. Without proper inspection methods it is almost impossible to determine whether particles are removed or not. In the following subsections three methods of inspection will be discussed, each with its own advantages and disadvantages. These methods are the conventional light microscope, the Nano Particle Detector (NPD), and the Scannning Electron Microscope (SEM).

### 5.3.1 Microscope

The simplest method of particle detection, is the inspection by a light microscope. Whenever it is possible, inspection by light microscope is preferred, since it is by far the most convenient method. The light microscope provides a fast and simple method of particle detection, and in most cases no special training is required to use the microscope. On the other hand, the light microscope is only suitable for the detection of relatively large particles. During the cleaning experiments it was found that the light microscope was able to reliably detect particles as small as 400 nm. The detection of smaller particles was not possible, and other techniques such as the Nano Particle Detector (NPD) and the Scanning Electron Microscope (SEM) were used instead.

### 5.3.2 Nano Particle Detector (NPD)

The second method of particle detection that will be discussed is the *Nano Particle Detector* (NPD), which was developed by TNO (Nederlandse organisatie voor Toegepast Natuurwetenschappelijk Onderzoek). Figure 5.7 shows a schematic sketch of how this

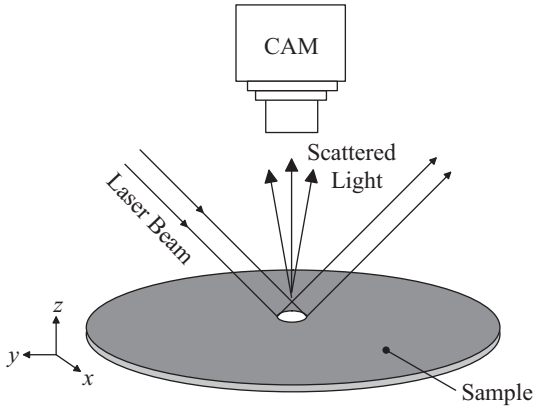


Figure 5.7: Working principle of the Nano Particle Detector (NPD). Particles on the surface of the sample scatter the light of the incident laser beam. The scattered light is recorded with a CCD camera above the sample.

particle detection tool works. During inspection, the sample is illuminated by a laser beam, and some of this laser light will be scattered due to the presence of particles on the surface of the sample. The scattered light, and thus the particle, is detected by a CCD camera above the sample. This method of detection is therefore only capable of detecting particles on unpatterned surfaces, since the presence of a pattern will also generate a lot of scattering. Because the sample is placed on a computer controlled $xyz$–stage, it is possible to inspect large areas with particles as small as 100 nm. Although it takes approximately six hours to scan a complete reticle, this is still a relatively short time when compared to inspection by the SEM. Unfortunately, the NPD is only able to detect the presence of a particle, and not its size. This means that one has to be very precise when preparing the particle samples, as not to contaminate the sample with particles of different sizes.

### 5.3.3 Scanning Electron Microscope (SEM)

Of all the detection methods discussed here, the Scanning Electron Microscope (SEM) is able to detect the smallest particles. On the other hand there are also a couple of disadvantages, such as the small field of view and its inability to inspect large areas within a reasonable amount of time. Using a SEM also requires special training, or the help of someone who is proficient in SEM operation. For these reasons the SEM is only used when all the other methods are incapable of detecting the particles.

## 5.4 Results of the Cleaning Experiments

For the first series of cleaning experiments, relatively large $SiO_2$ spheres (0.5–20 $\mu$m) were deposited on 1 inch wafers. Most of these particles were succesfully removed by applying 10 laser pulses of 350 mJ at a gap distance of 0.5, 1.0 and 1.5 mm. Gap distances below 0.5 mm were not possible, because of damage to the surface of the wafer. The degree of contamination before and after cleaning was determined with a light microscope. Figure 5.8 shows cleaning efficiency for each particle size and gap distance. In this case the

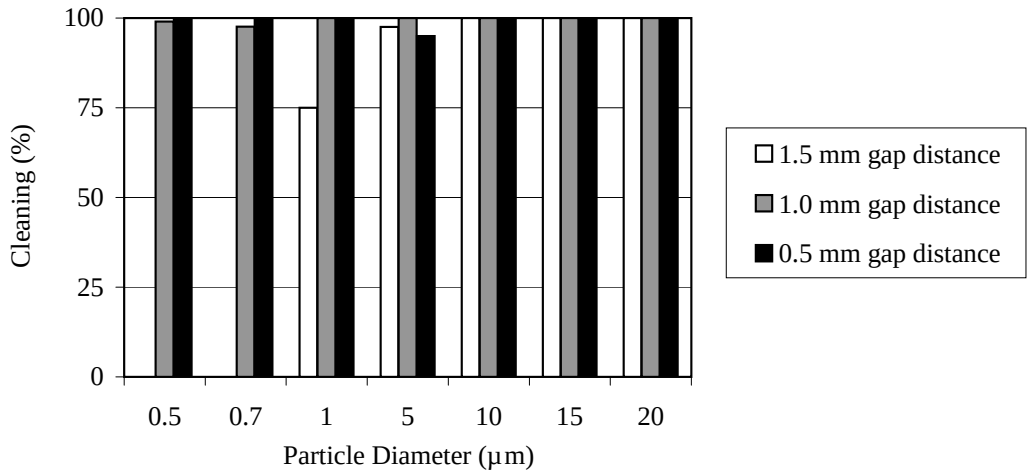


Figure 5.8: Overview of the measured cleaning efficiencies for various particle sizes and gap distances.

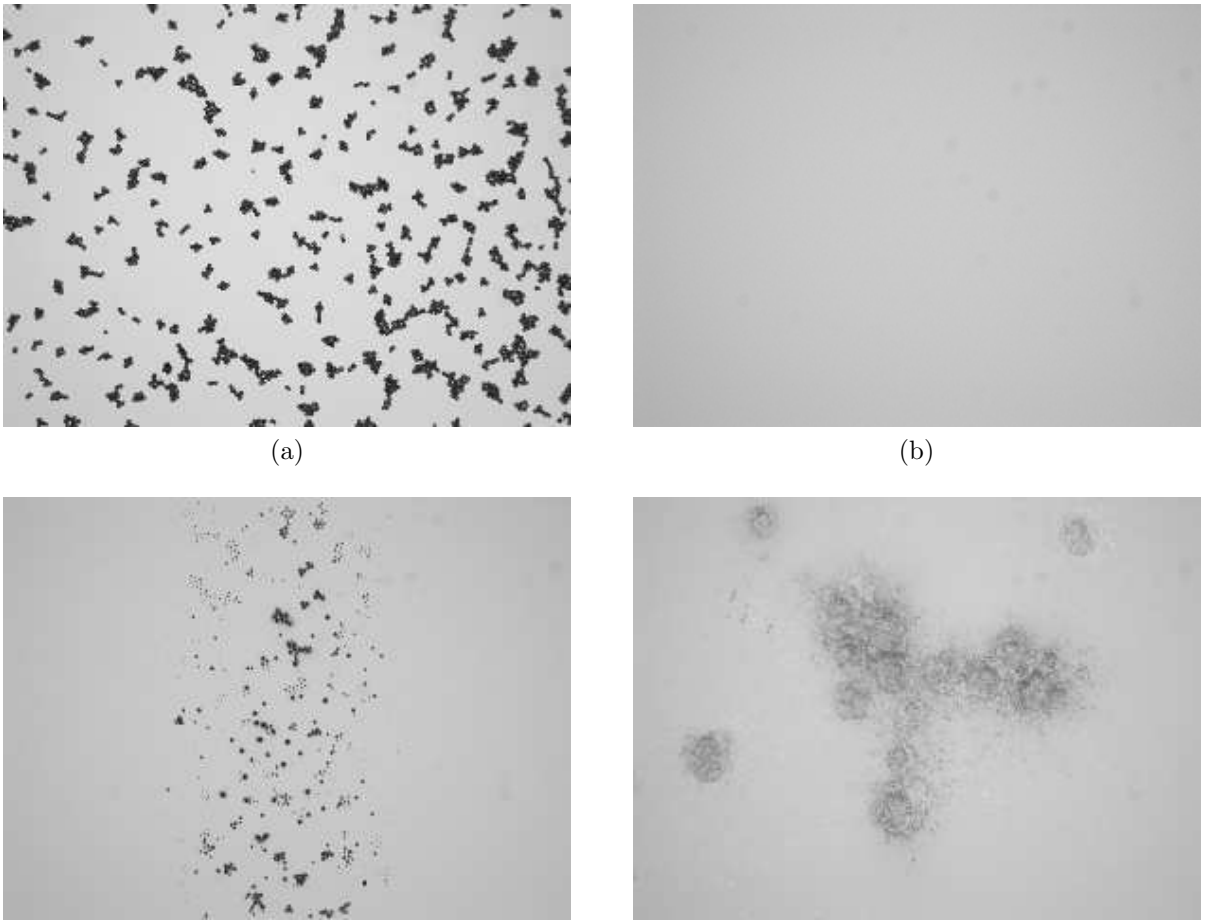


Figure 5.9: Microscope images (2.0×1.5 $mm^2$) of a sample with 20 $\mu$m $SiO_2$ spheres (a) before cleaning, and (b) after cleaning. Image (c) shows the surface of the sample directly beneath the laser focus. In this area there are still particles present, because the particles experience only a compressive force. (d) This compressive force is strong enough to pulverize the particles, as can be seen in this detailed image of the surface beneath the laser focus. This image is 200×150 $\mu m^2$ in size.

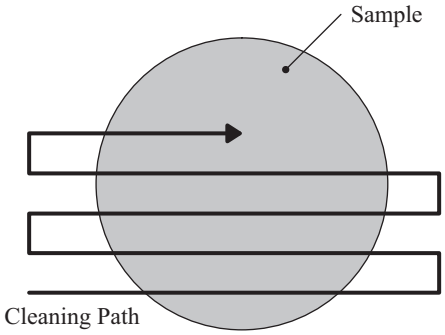


Figure 5.10: Example of a meandering cleaning path over the sample.

cleaning efficiencies were determined by counting the number of particles before and after cleaning. In some cases the particles directly beneath the laser focus could not be removed, because they do not experience a cleaning force. The particles in this elongated area are compressed by the shockwave, sometimes resulting in pulverized and possibly molten particles, as can be seen in figure 5.9. As expected, the damage to the particles decreases when the gap distance is enlarged. To mitigate this effect, the laser focus should not be directly above a part of the sample that has not already been cleaned by previous steps in the LSC process. In order to clean larger areas, this type of strategy will typically result in a meandering cleaning path over the surface of the sample (see figure 5.10).

The second series of cleaning experiments involved the removal of much smaller polystyrene latex (PSL) spheres (100–500 nm) from 1 inch silicon wafers. These particles are much more deformable than the $SiO_2$ particles from the previous experiment. It is therefore expected, that the PSL particles will be more difficult to remove than $SiO_2$ particles of the same size, because the increased contact area between the PSL spheres and the surface leads to a stronger van der Waals force. Furthermore, PSL spheres are used by many other experimenters worldwide for these type of experiments, which makes it a benchmark particle. In this case the cleaning procedure consisted of 10 laser pulses applied at a gap distance of 0.5 mm, after which the samples were scanned with the NPD. The results of these scans can be found in figure 5.11, and they show that all samples showed signs of cleaning. The scans also reveal what happens to the particles that are removed. This is particularly visible in the scan of the 500 nm particles. The darker ring around the cleaned area shows that the majority of the particles is redeposited nearby.

The third and final series of cleaning experiments were aimed towards the removal of very small PSL spheres (<100 nm), to find the diameter of the smallest particle that could be removed with the LSC setup. Since such small particles could not be detected by the NPD, these samples were inspected with the SEM. For these experiments a somewhat different cleaning strategy was adopted than for the previous experiments. In this case the LSC setup was used to clean a straight line across the sample, which was achieved by moving the sample underneath the laser focus. The SEM was then used to inspect the sample along a line, which was oriented perpendicular to the cleaned line (see figure 5.12). The results of these inspections can be found in figure 5.13. These graphs show the number of particles per SEM picture as a function of the position along the inspection line. These results show that it was possible to remove PSL particles as small as 50 nm.

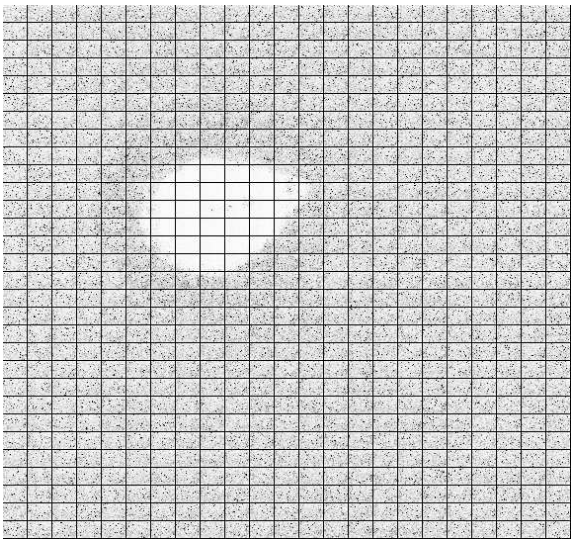

(a) 500 nm

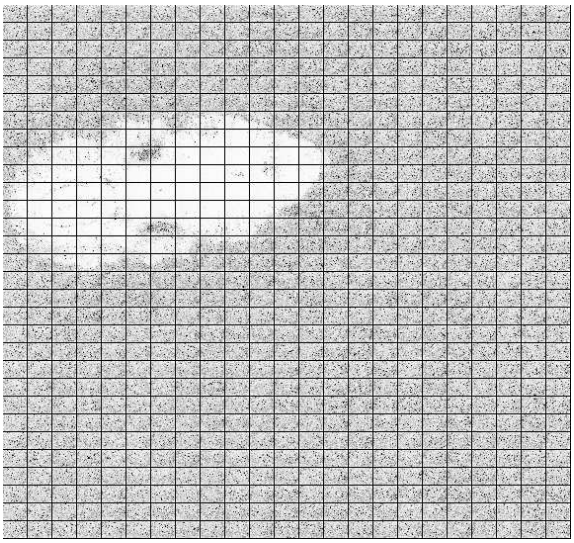

(b) 400 nm

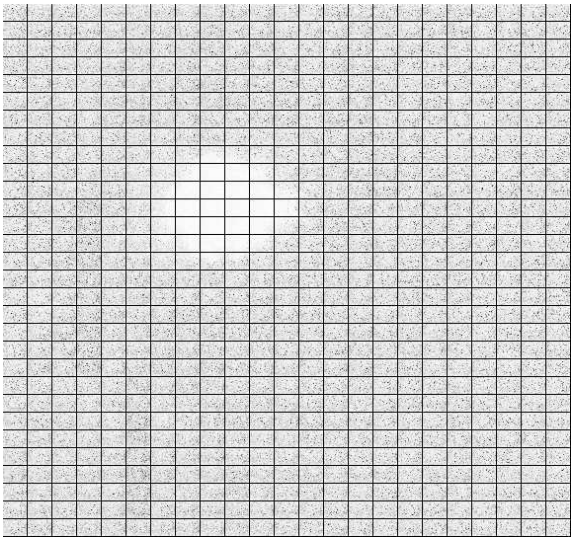

(c) 200 nm

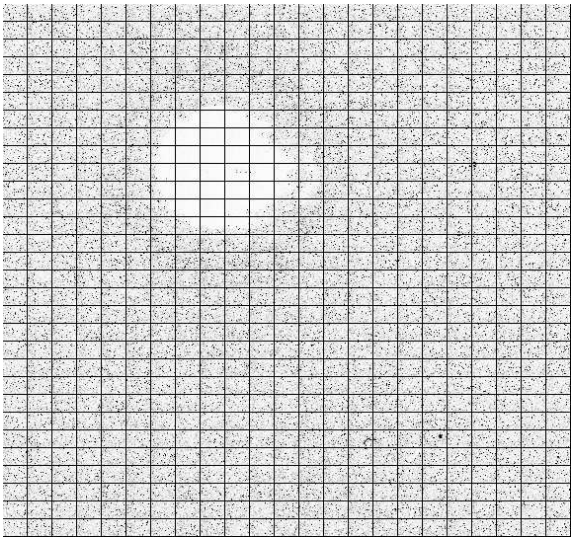

(d) 100 nm

Figure 5.11: Collection of scans made with the NPD, the dimensions of each image are $(15 \times 15)$ mm$^2$. The scan in subfigure (b) differs from the rest, because the sample was accidentally moved during cleaning. Also notice the dark rings around the cleaned area due to the redeposition of the removed particles.

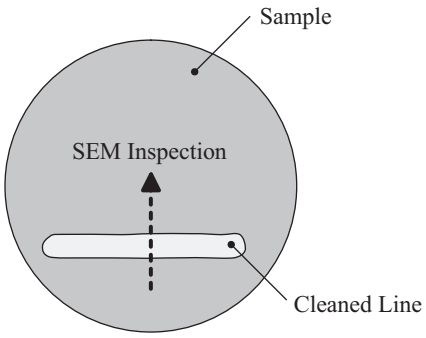


Figure 5.12: Schematic drawing of the line along which the sample was inspected with the SEM, during the third series of cleaning experiments.

Unfortunately, it was not possible to remove 30 nm particles, which is in agreement with the particle removal model presented in chapter 4.

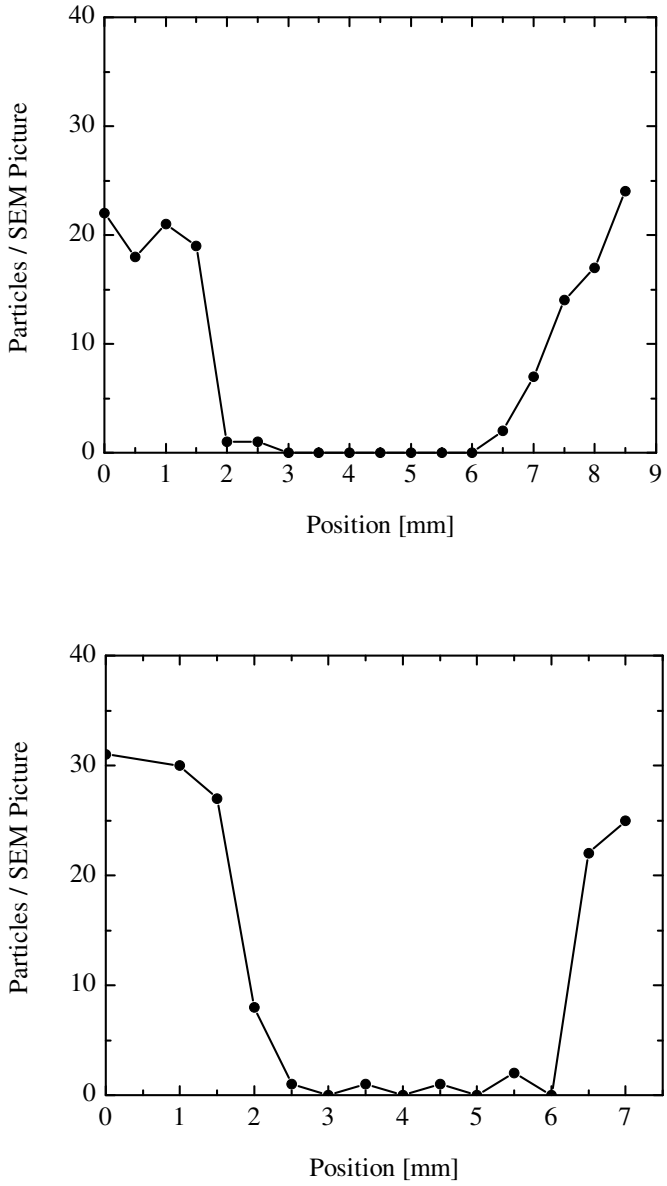


Figure 5.13: Two graphs showing the number of particles per SEM picture as a function of the position along the line of inspection. The first graph corresponds to a sample with 80 nm particles, and the second graph corresponds to a sample with 50 nm particles. Both graphs show clear signs of particle removal.

# 6 Conclusions and Remarks

## 6.1 Time Resolved Imaging

The time resolved imaging experiments in chapter 3 showed that the expansion of the shockwave generated by laser induced breakdown, is initially ellipsoidal, and not spherical as would be the case with a pure point explosion. Fortunately, it was still possible to describe the ellipsoidal expansion of the shockwave with a modified version of the Taylor & Sedov model [13] for point explosions. From the time resolved images it was possible to determine the amount of energy associated with the shockwave, which was found to be approximately 40% of the laser pulse energy. Furthermore, the time resolved images showed that the shockwave eventually degenerates into a normal sound wave. The interaction of the shockwave with a flat surface was also investigated. Here it was found that under specific circumstances it is possible, that the reflected shockwave combines with the original shockwave to form a so–called Mach stem.

## 6.2 Particle Removal Model

The particle removal model presented in chapter 4 was developed to predict the diameter of the smallest particle that can be removed with laser shockwave cleaning. The results of this model predicted that for the LSC setup used in this thesis, the diameter of the smallest removable particle has a value between 30 and 60 nm. This was later confirmed by the particle removal experiments presented in chapter 5. This prediction was however made under the assumption, that there are capillary forces present between the particle and the surface. When these capillary forces are eliminated from the model, the diameter of the smallest removable particle drops to a value well below 30 nm. This situation actually corresponds to the situation in an EUV lithography tool, where the water vapor pressure is too low to cause capillary condenstation. It is therefore recommended to continue the cleaning experiments in a water vapor free environment.

## 6.3 Cleaning Experiments

For reasons of cost-effectiveness and convenience, the cleaning experiments were performed on silicon wafers, instead of real EUV reticles. The main difference between a wafer and an EUV reticle, relevant to our experiments, is the presence of a pattern on the reticle. Small particles can easily hide inside the trenches of this pattern, and escape the full force of the shockwave. It is therefore expected, that the cleaning of a patterned surface will be more difficult than the cleaning of a smooth surface. Furthermore, it is also expected that the patterned surface of the EUV reticle will be more susceptible to damage. The successful cleaning of smooth surfaces can therefore be seen as a minumum requirement for the application of LSC in EUV reticle cleaning.

In the previous chapter it was shown, that it is possible to remove polystyrene latex particles down to 50 nm from a flat silicon surface with LSC. This result can be seen as a proof of concept for the LSC method, even though the removal of 30 nm particles was not yet possible. The particle removal model developed in chapter 4 predicts however, that

without capillary forces it might well be possible to remove particles smaller than 30 nm. Therefore, further cleaning experiments are needed to confirm this prediction.

In chapter 5 it was also shown, that there is one limiting factor that can severely limit the practical application of laser shockwave cleaning. This factor is the low repetition frequency at which the LIB and thus the shockwave can be created. This limitation will result in a very long cleaning time. The maximum repetition frequency can be increased by switching to a shorter wavelength laser to create the LIB, or by using a medium with a lower ionization potential. It is however doubtful that these adjustments will lead to a repetition frequency, that is high enough to make LSC a practical cleaning method for large surfaces. Another possible solution to this problem is the use of a short high intensity (but not necessarily high energy) prepulse to preionize the air, immediately followed by a secondary pulse which has sufficient energy to create a strong shockwave.

## 6.4 Recommendations for Future Research

Although the results of this study are encouraging, there is still a lot more work to be done. Now that the concept of laser shockwave cleaning is proven, it is time to see whether or not it is a practical cleaning method for EUV reticles. These experiments will involve the cleaning of much larger surfaces, and it is therefore recommended to use a computer controlled $xyz$–stage to move the sample around. As discussed in the previous subsections, these experiments should focus on the removal of particles smaller than 30 nm from patterned surfaces. Furthermore, it is recommended to switch to 300 mm wafers for the cleaning experiments, which makes it possible to use all the sophisticated detection and inspection tools available within ASML. Some of these inspection tools are even able to detect particles smaller than 30 nm on a patterned surface (KLA Tencor SurfScan).

# Bibliography

[1] G.E. Moore. Cramming more components onto integrated circuits. *Electronics*, 38(8), 1965.

[2] D. Attwood. *Soft X-Rays and Extreme Ultraviolet Radiation*. Cambridge University Press, 1999.

[3] International Technology Roadmap for Semiconductors (ITRS), http://www.itrs.net/.

[4] Center for X-Ray Optics (CXRO), http://www-cxro.lbl.gov/.

[5] A.L. Peratt. Advances in numerical modeling of astrophysical and space plasmas. *Astrophysics and Space Science*, 242(1–2):93–163, 1966.

[6] R. Engeln. Collegedictaat Inleiding Plasmafysica. University of Technology Eindhoven, 2005.

[7] C.G. Morgan. Laser-induced breakdown of gasses. *Reports on Progress in Physics*, 38:621–665, 1975.

[8] E. Toma. *Cluster Explosions and Characterization of Ultrashort XUV pulses*. PhD thesis, Vrije Universiteit Amsterdam, 2002.

[9] R. de Bruijn. *Dynamics of Laser Produced XUV Emitting Plasmas*. PhD thesis, Eindhoven University of Technology, 2004.

[10] M.E.H. van Dongen. Collegedictaat gasdynamica. University of Technology Eindhoven, 2004.

[11] M.A. Nettleton. *Gaseous Detonations*. Chapman and Hall Ltd, 1987.

[12] G.F. Kinney. *Explosive Shocks in Air*. Springer–Verlag, 1962.

[13] G.I. Taylor. The formation of a blast wave by a very intense explosion I. *Procedings of the Royal Society of London*, 201A(1065), 1950.

[14] W. Merzkirch. *Flow Visualization*. Academic Press, Inc., $2^{nd}$ edition, 1987.

[15] G.S. Settles. *Schlieren and Shadowgraph Techniques*. Springer–Verlag, 2001.

[16] T.P. Hughes. *Plasmas and Laser Light*. Adam Hilger, 1975.

[17] K. Mori. Energy transfer from a laser pulse to a blast wave in reduced–pressure air atmospheres. *Journal of Applied Physics*, 95(11), 2004.

[18] J. Israelachvili. *Intermolecular & Surface Forces*. Academic Press, 1985.

[19] Lecture Notes Particle Deposition, Transport & Removal, Clarkson University. Available online at http://www.clarkson.edu/projects/crcd/me437/index.php.

[20] B.V. Derjaguin. Untersuchungen über die Reibung und Adhäsion. *Kolloid Zeitschrift*, 69(2), 1934.

[21] H. Hertz. Über die Berürung Fester Elastischer Körper. *Journal für die reine und angewandte Mathematik*, 92:156–171, 1881.

[22] H.Krupp. Particle Adhesion Theory and Experiment. *Journal of Advanced Colloid Interface Science*, 1, 1967.

[23] A.D. Roberts K.L. Johnson, K. Kendall. Surface energy and the contact of elastic solids. *Proceedings of the Royal Society of London*, 324(1558):301–313, 1971.

# A Particle Removal Model Source Code

```
%%%%%%%%%%%%%%%%%%%%%%%%%%%%%%%%%%%%%%%%%%%%%%%%%%%%%%%%%%%%%%%%%%%%%%%%%%%%%%%%
% script:                                                                       %
%     lscsim.m                                                                  %
% description:                                                                  %
%     calculates the diameter of the smallest removable PSL sphere              %
%     on a flat silicon surface for a range of gap distances and                %
%     shockwave energies                                                        %
% author:                                                                       %
%     niels lammers, nov 2007                                                   %
%%%%%%%%%%%%%%%%%%%%%%%%%%%%%%%%%%%%%%%%%%%%%%%%%%%%%%%%%%%%%%%%%%%%%%%%%%%%%%%%

clear all

%%%%%%%%%%%%%%%%%%%%%%%%%%%%%%%%%%%%%%%%%%%%%%%%%%%%%%%%%%%%%%%%%%%%%%%%%%%%%%%%
% initialize constants                                                          %
%%%%%%%%%%%%%%%%%%%%%%%%%%%%%%%%%%%%%%%%%%%%%%%%%%%%%%%%%%%%%%%%%%%%%%%%%%%%%%%%

E_s = 190e9;                    % Young modulus [Pa] of the surface
E_p = 2.3e9;                    % Young modulus [Pa] of the particle
nu_s = 0.17;                    % poisson ratio [-] of the surface
nu_p = 0.35;                    % poisson ratio [-] of the particle

gamma_L = 72e-3;                % surface tension [N/m] of water
gamma = 1.4;                    % specific heat ratio [-] of air
Y = 1.03;                       % empirical t&s constant [-] of air

A = 12.2e-20;                   % hamaker constant [J] (psl-air-si)
D = 4e-10;                      % seperation distance [m]
Wa = A/(12*pi()*D^2);           % thermodynamic work of adhesion [J/m2]

K = 4/3*((1-nu_s^2)/E_s+(1-nu_p^2)/E_p)^(-1); % elastic constant [Pa]

%%%%%%%%%%%%%%%%%%%%%%%%%%%%%%%%%%%%%%%%%%%%%%%%%%%%%%%%%%%%%%%%%%%%%%%%%%%%%%%%
% iterative procedure to find the smallest removable particle                   %
% diameter as a function of the shockwave energy W and gap                      %
% distance g                                                                    %
%%%%%%%%%%%%%%%%%%%%%%%%%%%%%%%%%%%%%%%%%%%%%%%%%%%%%%%%%%%%%%%%%%%%%%%%%%%%%%%%

step = 0;

for i=1:100
```

```
% calculate shockwave energy W [J]
W = i*2.5e-3;

for j=1:100

    % calculate gap distance g [m]
    g = j*0.25e-4;

    % keep track of the number of iteration steps
    step = step+1;
    msg = sprintf('%u of 10000',step);
    disp(msg);

    % reset the cleaning indicator
    cleaning = false;

    % initialize smallest removable particle radius
    Rmin = 500e-9;

    for k=1:1000

        % calculate particle radius R [m]
        R = k*0.5e-9;

        a_0 = (6*pi()*R^2*Wa/K)^(1/3);

        for l=1:101

            % calculate distance x [m] between
            % ground zero and the particle
            x = (l-1)*1e-4;

            % initialize residues and tolerance
            residue1 = 1e10;
            residue2 = 1e10;
            tolerance = 1e-10;

            % estimate the contact radius
            % and the deformation length
            a = 0.1*R;
            delta = a^2/R;

            while (residue1>tolerance | residue2>tolerance)

                % calculate distance r [m] from focus to particle
                r = sqrt((g-R+delta)^2 + x^2) - R;
```

```
    % calculate usefull goniometric relations
    sin_theta = (g-R+delta)/(R+r);
    cos_theta = x/(R+r);

    % calculate pressure jump dp [Pa]
    % across the shockwave
    dp = 8/25*W/r^3*Y^5/(gamma+1);

    % calculate shockwave force
    % F [N] and its components
    Fs = pi()*R^2*dp;
    Fn = Fs*sin_theta;
    Fp = Fs*cos_theta;

    % calculate the capillary force Fc [N]
    Fc = 4*pi()*R*gamma_L;

    % calculate the external load
    % P [N] applied to the particle
    P = Fc+Fn;

    % save the old value of a
    % before computing the next one
    a_old = a;

    % calculate jkr contact radius a [m]
    a = (R/K*(P+3*Wa*pi()*R+sqrt(6*Wa*pi()*R*P
        +(3*Wa*pi()*R)^2)))^(1/3);

    % save old value of delta
    % before computing the new one
    delta_old = delta;

    % calculate deformation length delta [m]
    delta = a^2/R*(1-2/3*(a_0/a)^(3/2));

    % calculate the residues [-]
    residue1 = abs(1-a_old/a);
    residue2 = abs(1-delta_old/delta);

end % while loop

% calculate adhesion force Fa [N]
Fa = A*R/(6*D^2)*(1+a^2/(R*D));

% calculate cleaning moment Mc[Nm]
hy = R-delta+R*sin_theta;
```

```
                Mc = Fp*hy;

                % calculate adhesion moment Ma[Nm]
                hx = R*cos_theta;
                Ma = Fn*(hx+a)+Fa*a+Fc*a;

                % calculate moment ratio [-]
                Mratio = Mc/Ma;

                % check for cleaning
                if (Mratio>1.0)
                    cleaning = true;
                    break;
                end

            end % x loop

            % save smallest removable particle radius
            if (cleaning==true)
                Rmin = R;
                break;
            end

        end % R loop

        % save the results
        X_data(i,j) = g;
        Y_data(i,j) = W;
        Z_data(i,j) = Rmin;

    end % g loop

end % W loop

% write the results to a csv file
X = reshape(X_data,1,10000)';
Y = reshape(Y_data,1,10000)';
Z = reshape(Z_data,1,10000)';
CSV_data = [X Y Z];
csvwrite('result.csv',CSV_data);
```

# Acknowledgements

Although it might sound as a cliché, this work would not have been possible without the help of other people. Here at the end of my thesis, I would like to take a minute and thank all the people that have helped and supported me during the past year. First of all, I would like to thank my two supervisors Arno Bleeker and Joost van der Mullen for their help and support. Many thanks also to Luigi Scaccaborozzi for his help with the cleaning experiments and the SEM. My thanks also go to Sjoerd Donders and Rogier Cortie, for letting me use their laser for the imaging experiments. I am also thankful for the help I received from Luc Steevens and John de Kuster whenever I needed parts or equipment. Furthermore, I would like to thank Eddie van Veldhuizen, who kindly supplied me with the iCCD camera for the imaging experiments. Many thanks also to Jetske Stortelder and Jacques van der Donck from TNO Delft for their assistance in the preparation of the particle samples. And finally, I would like to thank my parents for their years of unconditional help and support.